uOttawa

L'Université canadienne
Canada's university

FACULTÉ DES ÉTUDES SUPÉRIEURES ET POSTOCTORALES

uOttawa

L'Université canadienne
Canada's university

FACULTY OF GRADUATE AND POSDOCTORAL STUDIES

Jesse Leeson
AUTEUR DE LA THÈSE / AUTHOR OF THESIS

M.Sc. (Physics)
GRADE / DEGREE

Department of Physics
FACULTÉ, ÉCOLE, DÉPARTEMENT / FACULTY, SCHOOL, DEPARTMENT

The Dynamics of Polarization in Communication Fiber
TITRE DE LA THÈSE / TITLE OF THESIS

X. Bao
DIRECTEUR (DIRECTRICE) DE LA THÈSE / THESIS SUPERVISOR

CO-DIRECTEUR (CO-DIRECTRICE) DE LA THÈSE / THESIS CO-SUPERVISOR

D. Asner

E. Fortin

P. Lu

Gary W. Slater
Le Doyen de la Faculté des études supérieures et postdoctorales / Dean of the Faculty of Graduate and Postdoctoral Studies

The Dynamics of Polarization in Communication Fiber

Jesse Leeson

Thesis submitted to the
Faculty of Graduate and Postdoctoral Studies
In partial fulfillment of the requirements
For the M.Sc. degree in Physics

Department of Physics
Faculty of Science
University of Ottawa

Your file Votre référence
ISBN: 978-0-494-61216-3
Our file Notre référence
ISBN: 978-0-494-61216-3

Table of Contents

List of Figures

List of Abbreviations

APD:	Avalanche Photodiode
BER:	Bit Error Rate
DAQ:	Data Acquisition
DC:	Direct Current
DGD:	Differential Group Delay
DUT:	Device Under Test
DOP:	Degree Of Polarization
DSF:	Dispersion Shifted Fiber
EDFA:	Erbium Doped Fiber Amplifier
OFCS:	Optical Fiber Current Sensor
FRM:	Faraday Rotation Mirror
FUT:	Fiber Under Test
FWHM:	Full Width at Half Maximum
OCT:	Optical Coherence Topography
MMF:	Multi Mode Fiber
NZ:	Non-Zero
OFDR:	Optical Frequency Domain Reflectometery
OPGW:	Optical Ground Wire Network
OSA:	Optical Spectrum Analyzer
OTDR:	Optical Time Domain Reflectometery
PDL:	Polarization Dependent Loss
PMD:	Polarization Mode Dispersion
POTDR:	Polarization Optical Time Domain Reflectometery

PSP:	Principle State of Polarization
PZT:	Piezoelectric Transducer
SMF:	Single Mode Fiber
SOP:	State Of Polarization

Abstract

Here a temperature stable optical fiber current sensor based on the Sagnac loop interferometer and a cavity formed from two Faraday rotation mirrors is developed and tested. To the best of the author's knowledge a cavity composed of two Faraday rotation mirrors has never been used for the measurement of alternating currents.

For the first time, it is shown that the maximum Faraday rotation angle for a long, static optical fiber is input polarization insensitive. Also, linear birefringence is shown to quench this angle in long optical fiber.

The polarization dynamics in an optical ground wire network, for a summer period and a fall period, are reported for the first time. The highest-speed polarization changes are attributed to the high-voltage power line, i.e., the electrical current.

A novel spectral analysis polarization optical time domain reflectometry method, that uses an induced birefringent event, is shown to work in long optical fiber.

Acknowledgements

I would like to thank my supervisor, Dr. Xiaoyi Bao, for her constant guidance and support. Her innovation and work ethic have been both motivating and inspiring for me. It has been an honour to be a member of her research team. The completion of my thesis could have never occurred without our discussions.

Also, I thank Dr. Alain Cote for all our excellent conversations on field and lab work. Our collaborations made a tremendous contribution to my thesis. His acute attention to detail has helped keep my work on track, time and time again.

My colleagues from the Fiber Optics Group, both past and present, have also contributed greatly to my work: I thank Dr. John Cameron for my introduction to optical fiber and assistance in getting started with my endeavors. I would also like to thank Ryan Bolen for his assistance in the lab with equipment and ordering. My discussions with him, and his knowledge of electronics, have been great assets. Also, I thank Dr. Ziyi Zhang for our discussions on many polarization topics.

Statement of Originality

This work contains no material which has been accepted for the award of any other degree or diploma in any university or other tertiary institution and, to the best of my knowledge and belief, contains no material previously published or written by another person, except where due reference has been made in the text.

I give consent to this copy of my thesis, when deposited in the University Library, being available for loan and photocopying.

SIGNED: ..Jesse Leeson.....

DATE: .....Dec. 04 / 09.....

Supervisor: Prof. Xiaoyi Bao

Chapter 1

Introduction

The state of polarization (SOP) of an electromagnetic wave describes how the amplitude and phase of the electric field are behaving at a particular position in space. By measuring the SOP of light emitted from media, important information is gained about its optical properties. The measurement and study of polarization is known as polarimetry. Experimentally, the SOP of light is described using four parameters called the Stokes parameters.

1.1 Mathematical Description of Polarization

Stokes Space

Stokes space is a three-dimensional real vector space. It effectively describes polarized light, partially polarized light, and non-polarized light. The Stokes vector is written as $\vec{S} = [S_o, S_1, S_2, S_3]$ where the Stokes parameters are defined as (Goldstein, 2003):

$$\begin{aligned} S_o &= |E_{ox}|^2 + |E_{oy}|^2 \\ S_1 &= |E_{ox}|^2 - |E_{oy}|^2 \\ S_2 &= 2E_{ox}E_{oy}\cos\varphi \\ S_3 &= 2E_{ox}E_{oy}\sin\varphi \end{aligned}, \qquad (1.1)$$

where $E_x = E_{ox}\exp(j\varphi_x)$ is the x-direction and $E_y = E_{oy}\exp(j\varphi_y)$ is the y-direction complex components of the lights electric field as it propagates in the z-direction and $\varphi = \varphi_y - \varphi_x$. Experimentally, it is more convenient to re-express the Stokes parameters in terms of the intensity using a spherical coordinate system (Zhang, 2007):

$$\begin{aligned} S_o &= I \\ S_1 &= Ip\cos 2\varepsilon \cos 2\theta \\ S_2 &= Ip\cos 2\varepsilon \sin 2\theta \\ S_3 &= Ip\sin 2\varepsilon \end{aligned}, \qquad (1.2)$$

where I is the intensity, p is the degree of polarization (DOP), and Ip is the radial spherical coordinate where θ and ε are polar coordinates are related by:

$$\theta = \frac{1}{2}\tan^{-1}\left(\frac{S_2}{S_1}\right), \tag{1.3}$$

$$\varepsilon = \frac{1}{2}\sin^{-1}\left(\frac{S_3}{\sqrt{S_1^2+S_2^2+S_3^2}}\right), \tag{1.4}$$

The DOP is the ratio of polarized light intensity to the total light intensity and is defined in term of the Stokes parameters as:

$$p = \frac{\sqrt{S_1^2+S_2^2+S_3^2}}{S_o}, \tag{1.5}$$

In the case of totally polarized light $p = 1$, for partially polarized light $0 < p < 1$, and for non-polarized light $p = 0$. The Stokes parameters are found using easily measured experimental quantities, i.e., light intensities.

To interpret the Stokes parameters, it is convenient to observe the termination point of the normalized Stokes vector on a unit sphere in Stokes space. This unit sphere is called the Poincare sphere. Normalization of the Stokes vector allows even partially polarized light to be represented as a point on the surface of the Poincare sphere. A point plotted on the Poincare sphere at a given time represents the instantaneous SOP of light. Every point plotted on the Poincare sphere is a unique SOP. The Poincare sphere is displayed in figure 1.1.

The SOP often evolves as a lightwave propagates through an optical medium. There are two formalisms for describing the polarization evolution of light as it propagates through such a medium: Jones calculus and Mueller calculus.

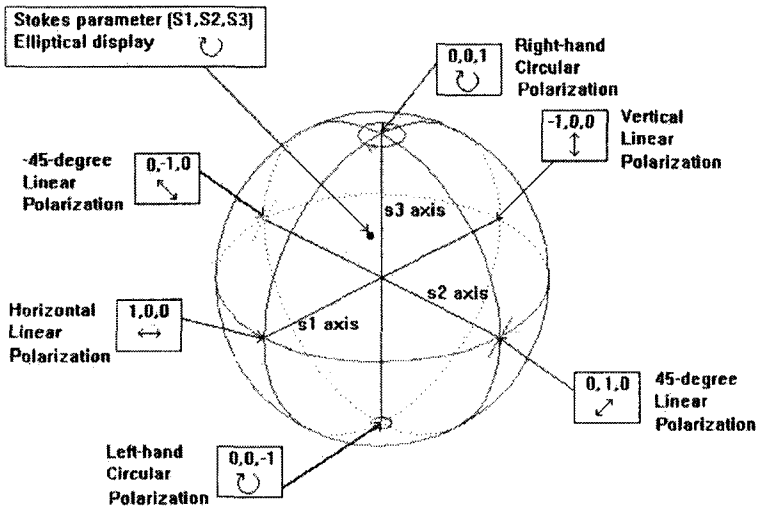

Figure 1.1 The Poincare sphere displaying the degenerate SOP and an elliptical SOP (from Agilent Technologies, 2001)

Jones Calculus

Jones calculus describes the SOP of light using a column vector referred to as the Jones vector:

$$\begin{bmatrix} E_x \\ E_y \end{bmatrix}, \tag{1.6}$$

where $E_x = E_{ox}\exp(j\varphi_x)$ is the x-direction and $E_y = E_{oy}\exp(j\varphi_y)$ is the y-direction complex components of the light's electric field as it propagates in the z-direction. The intensity is then described by $I = E_x E_x^* + E_y E_y^*$. The Jones vector is usually written in normalized form.

To describe the evolution of the SOP through a medium, an associated $2x2$ matrix is used. This matrix is called the Jones transfer matrix. It operates on the initial Jones vector to find the final Jones vector. Each transfer matrix is wavelength dependent. The Jones vector cannot describe partially polarized light; however, the phase information is maintained.

Mueller Calculus

Mueller calculus describes the SOP of light using the Stokes vector written as a column vector. The Mueller transfer matrix is a $4x4$ real component matrix. Similar to Jones calculus, the Mueller transfer matrix represents the SOP evolution through a medium. The Mueller transfer matrix is directly applied to the Stokes vector to find the output Stokes vector. Mueller calculus becomes very useful in experiment because it uses the Stokes vector and the Mueller transfer matrix, which are calculated from experimentally measured intensities. Mueller transfer matrices are also wavelength dependent.

Mueller calculus can be more inconvenient than the Jones calculus method because the Mueller transfer matrix contains twice the elements the Jones transfer matrix does. An important advantage of Mueller calculus, however, is that it can describe partially polarized light. Mueller calculus is over-determined in the event that there is no light depolarization.

1.2 Polarimetry

Polarizers are required to determine the SOP of light in polarimetry. They act as filters because they have a preferential SOP of transmission. For an incident beam of arbitrary SOP, only the projection of the Stokes vector onto the preferential Stokes vector is transmitted. The transmitted intensity is then dependent on the original SOP of the light. The intensity can be measured using an optical detector. If the SOP measurement is recorded over a given time interval, the dynamic optical properties of the medium can be observed. Also, if the original polarization of the light is known, the evolution of the SOP through the optical medium can be determined.

A basic polarization analyzer uses four stationary polarization filters to dynamically measure the SOP of light. This type of polarization analyzer contains a four-way beam

splitter, four polarization filters, and four photodiode detectors for simultaneous recording of the intensity of the transmitted light. The internal diagram of a commercial Agilent 8509B polarization analyzer is shown in figure 1.2. The Agilent 8509B has a maximum acquisition speed of $2\ kHz$; however, other polarization analyzer designs vary in acquisition speed from direct current (DC)-GHz. Polarization analyzers with acquisition speeds of GHz are more common in astronomy because observation of some pulsars can require a minimum of $10\ kHz$ sampling rate (Phelan, 2007). The design of an ultra-high-speed polarization analyzer must use no moving parts and very fast detectors to measure all four Stokes parameters simultaneously (Phelan, 2007).

The intensities measured by the polarization analyzer are I_o, I_1, I_2, and I_3. I_o is the measured intensity after the light signal travels through an air gap or glass plate, I_1 is the measured intensity after passing through a horizontal linear polarizer, I_2 is the measured intensity after passing through a linear polarizer oriented at 45^o, and I_3 the measured intensity after passing through a quarter wave plate that induces a $\pi/2$ phase shift, rendering circularly polarized light to linearly polarized light, and then a linear polarizer oriented at 45^o. The following Mueller transfer matrix is then used to find the Stokes vector (Damask, 2004):

$$\begin{bmatrix} S_o \\ S_1 \\ S_2 \\ S_3 \end{bmatrix} = \begin{bmatrix} 1 & 0 & 0 & 0 \\ -1 & 2 & 0 & 0 \\ -1 & 0 & 2 & 0 \\ -1 & 0 & 0 & 2 \end{bmatrix} \begin{bmatrix} I_o \\ I_1 \\ I_2 \\ I_3 \end{bmatrix}, \tag{1.7}$$

where $I_o = |E_{ox}|^2 + |E_{oy}|^2$.

In the next chapter, the fundamentals of optical fiber will be reviewed. This discussion is critical for the understanding of the polarization properties of optical fiber.

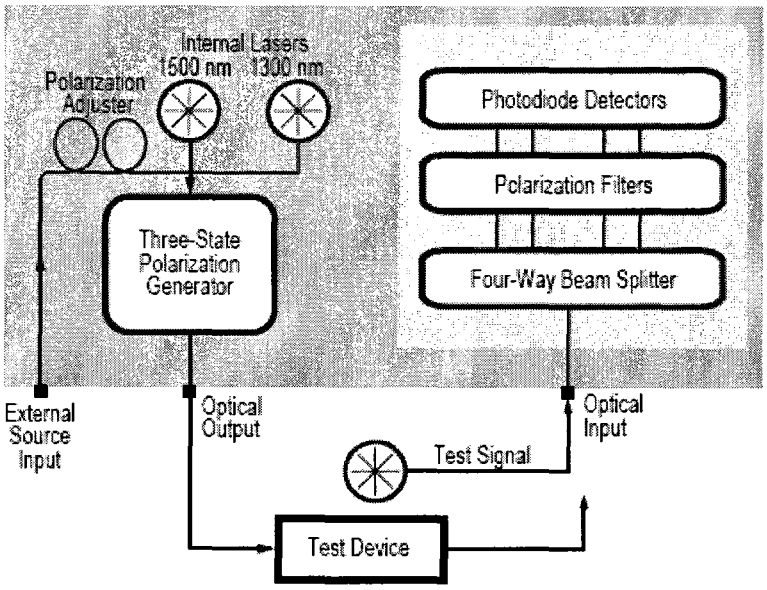

Fig 1.2 The internal diagram of the Agilent 8509B polarization analyzer (from Agilent Technologies, 1993)

Chapter 2

Polarization in Optical Fiber

2.1 Optical Fiber

Optical fiber has revolutionized the communication industry over the last half-century. It began to dominate because of its lower loss than copper wire and higher bandwidths than either copper wire or microwave communication systems. Advancements in the optical fiber manufacturing processes during the 1970's led to the highly competitive low-loss optical fibers used in modern day communications. Optical fiber impurities were no longer a major limiting factor in optical fiber transmission.

Figure. 2.1 shows theoretical spectral loss contributions and experimental spectral loss for a typical communication fiber. Rayleigh scattering is shown to dominate optical fiber loss. Note the window of lower loss at the modern day communication wavelength, $1550\ nm$, where the absorption and scattering become minimum.

There are two types of optical fiber: single mode fiber (SMF) and multi mode fiber (MMF). SMF only guides one mode of light and the core diameter is often on the same scale as the wavelength of optical light. However, MMF usually has a large core and can guide hundreds of optical modes. SMF has a major advantage over MMF because it does not experience modal dispersion as MMF does, giving it a much higher bandwidth. The modal dispersion in MMF results from each beam having different coupling angles; the variations lead to path differences in the light propagation. For this reason, SMF dominates the communication industry and here SMF will be focused on and not MMF.

A typical SMF uses a step index profile as shown in figure 2.2. To manufacture a step index SMF, a relationship between wavelength, dimensions, and refractive index is

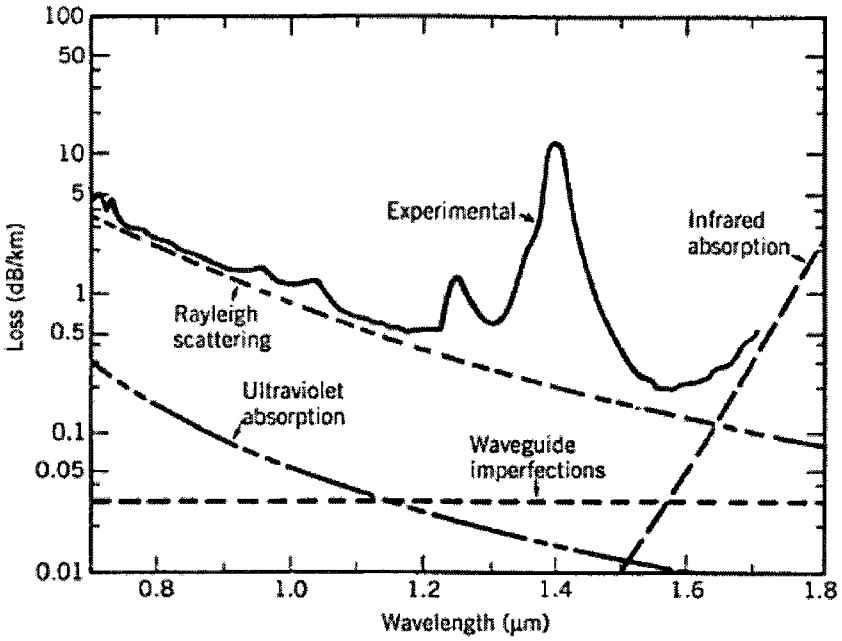

Figure 2.1 The experimental (solid line) and theoretical optical fiber loss (dotted line) vs. wavelength (from Agrawal, 2002).

required. For this it is helpful to define the parameter V at a given wavelength:

$$V = k_o a(n_1^2 - n_2^2)^{\frac{1}{2}}, \tag{2.1}$$

where $k_o = 2\pi/\lambda$ is the angular wave number, a is the core radius, n_1 and n_2 are the refractive index for the core and cladding respectively, and λ is the wavelength of the light being transmitted. It is known that for $V < 2.405$ (Agrawal, 2001) the optical fiber will be a SMF. To ensure propagation (total internal reflection), the refractive index, n_1, must be higher than the refractive index, n_2. Typically, n_1 is around $1.44 - 1.46$, while n_2 is determined by the relative core-cladding index difference, $\Delta = (n_1 - n_2)/n_1$. For SMF $\Delta \approx 0.003$. Considering all parameters, a typical value of the core radius, a, is $< 5\ \mu m$ and cladding radius, b, is $\sim 62.5\ \mu m$. A jacket of refractive index n_0 is often added to protect the

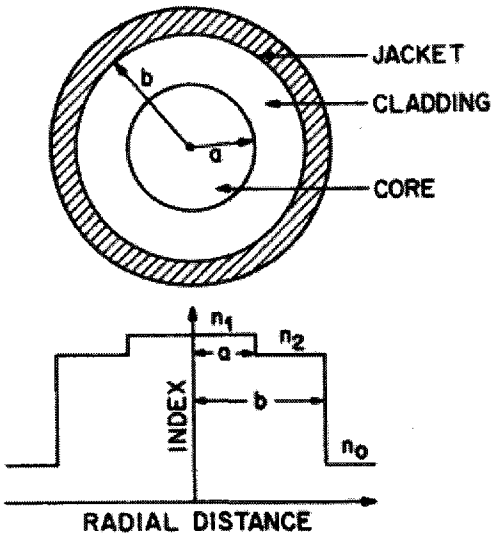

Figure 2.2 A schematic cross section and refractive index profile of a typical step index optical fiber (from Agrawl, 2001).

optical fiber. The choice of jacket material depends on the operating environment. In some instances a jacket is not added and n_0 is the refractive index of air.

It is important to note that while extreme care is used in the fabrication and installation process of optical fibers, an ideal optical fiber cannot be manufactured. In the next section, the natural consequence of these flaws will be introduced, a property called birefringence.

2.2 Birefringence, PMD, and PDL in Optical Fiber

Birefringence

Ideally, optical fiber is perfectly symmetric and isotropic, as shown in figure 2.2. However, optical fiber has imperfections and intrinsic stress. Therefore, optical fiber is

generally anisotropic due to the manufacturing and installation process. This causes an asymmetric refractive index profile and essentially birefringence.

A linear birefringent material has two directional axes and thus SMF actually has two propagation modes, one along each axis. The two modes propagate at different speeds due to the refractive index difference. This results in a constant evolution of the propagating light beam's polarization. The axis that experiences the faster propagation constant defines the fast polarization axis and the slower propagation constant defines the slow polarization axis. Linear birefringence is defined as:

$$\Delta\beta = |\beta_x - \beta_y| = \frac{2\pi B_M}{\lambda}, \tag{2.2}$$

where β_x and β_y are, in no preferential order, the propagation constants for the fast and slow axes, $B_M = |n_x - n_y|$ is the linear modal birefringence, λ is the wavelength of the light source, and the lightwave is traveling in the z-direction.

A constant linear birefringence leads to a periodic evolution of the SOP in the optical fiber where $\Delta\beta z = 2\pi$ is the condition for a given SOP to return to its original state. For a given optical fiber the periodic SOP evolution is characterized by the polarization beat length, L_B, defined by:

$$L_B = \frac{2\pi}{|\beta_x - \beta_y|} = \frac{\lambda}{B_M}, \tag{2.3}$$

An example of the polarization beat length is illustrated in figure 2.3.

As shown in equations 2.2 and 2.3, linear birefringence and the polarization beat length are functions of wavelength. Therefore, small modulations in a light sources wavelength will change the SOP evolution in the same optical fiber length. The SOP evolution is altered when the linear birefringence increases or decreases and the output SOP still reoccurs with a constraint of $\Delta\beta z = 2\pi$. From it is determined that the SOP

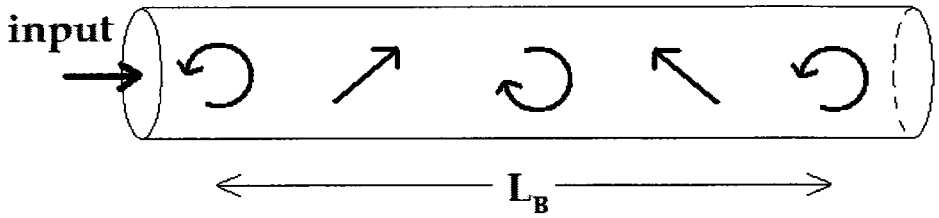

Figure 2.3 A visualization of the 2π evolution of a circular SOP back to its original state, representing one polarization beat length of this optical fiber.

evolution is also periodic with wavelength change for an optical fiber of constant length. In fact, a variation in wavelength or optical fiber length produces the same SOP change in optical fiber (Menyuk, 2005).

An important exception to polarization beating in optical fiber is the principle state of polarization (PSP). For an optical fiber of constant linear birefringence, any linear SOP launched entirely along either the fast or slow axis will not experience any polarization mode coupling, and the output SOP will be the same as the original SOP regardless of propagation length. By definition, the two PSP are orthogonal at the input and output of the optical fiber and because they are not affected by linear birefringence they are invariant with frequency.

Until now, I have only discussed linear birefringence, which tends to be dominant in typical communication optical fiber. In reality, there are two fundamental types of birefringence in optical fiber: linear birefringence and circular birefringence. Linear birefringence causes the two linear polarization modes to travel at different speeds, as is the case with a linear retarder. Circular birefringence causes the left and right-handed polarization modes to travel at different speeds, as is the case with a circular retarder. Circular birefringence is simply the circular equivalent to linear birefringence with β_x and β_y replaced by β_L and β_R. Examples of induced linear birefringence include: lateral

compression, bending, and electric field exposure. Examples of circular birefringence include: twisting and longitudinal magnetic field exposure (Chen, 2006). The combination of linear and circular birefringence, which is the case with twisted SMF, is called elliptical birefringence.

Considering an optical fiber with only a constant linear birefringence, the optical fiber can be modeled as a phase retarder using the following Jones transfer matrix:

$$\begin{bmatrix} \exp\left(\frac{j\Delta\beta z}{2}\right) & 0 \\ 0 & \exp\left(-\frac{j\Delta\beta z}{2}\right) \end{bmatrix}, \tag{2.4}$$

where $\Delta\beta$ is the linear birefringence in radians/m, and the vertical axis is the fast axis. In the case of only circular birefringence, the SOP evolution is modeled as an SOP rotation using the following Jones transfer matrix:

$$\begin{bmatrix} \cos(\Delta\beta_C z) & -\sin(\Delta\beta_C z) \\ \sin(\Delta\beta_C z) & \cos(\Delta\beta_C z) \end{bmatrix}, \tag{2.5}$$

where $\Delta\beta_C$ is the circular birefringence in radians/m, and a right-hand rotation is positive. Elliptical birefringence can then be described using the following Jones transfer matrix (Smith, 1980):

$$\begin{bmatrix} \cos\left(\frac{\phi z}{2}\right) + j\frac{\Delta\beta}{\phi}\sin\left(\frac{\phi z}{2}\right) & -\frac{2\Delta\beta_C}{\phi}\sin\left(\frac{\phi z}{2}\right) \\ \frac{2\Delta\beta_C}{\phi}\sin\left(\frac{\phi z}{2}\right) & \cos\left(\frac{\phi z}{2}\right) - j\frac{\Delta\beta}{\phi}\sin\left(\frac{\phi z}{2}\right) \end{bmatrix}, \tag{2.6}$$

where $\phi^2 = \Delta\beta^2 + (2\Delta\beta_C)^2$. This expression shows how elliptical birefringence in optical fiber results from the superposition of linear and circular birefringence. For completeness, if $\Delta\beta_C = 0$, equation 2.6 recovers the expression for the linear birefringence case, as shown in equation 2.4; if $\Delta\beta = 0$, equation 2.6 recovers the circular birefringence case, as shown in equation 2.5.

Intuitively, one can assume that passing through a birefringent medium, be it linearly, circularly, or elliptically birefringent, in one direction can produce a SOP change that is removable by passing through the medium in the reverse direction. In fact, for most birefringence in optical fiber, i.e. bending, twisting, etc., when a light beam is orthogonally transmitted in the reverse direction through the same birefringence, the SOP change is reciprocal. However, not all birefringent effects are reciprocal. Most notably the Faraday effect, which results from longitudinal magnetic field exposure, is a non-reciprocal circular birefringence. An orthogonally reverse propagating beam will undergo the same SOP change the counter propagating beam experiences. The reciprocal and non-reciprocal properties of optical fiber birefringence will be exploited later in the text.

PMD and PDL

Birefringence has an important consequence to pulse propagation in optical fiber, particularly in the field of communications. A natural result of birefringence is that when a pulse is launched containing both fast and slow PSP, the components will experience different group delays as they propagate through an optical fiber. The random variations in the optical fibers birefringence will then lead to random-walk of the pulse's polarization components. The group delay difference of the two PSP is known as differential group delay (DGD) and is measured in units of ps.

Another measure of DGD is the maximum broadening of a broadband pulse. In communications, pulses are composed of many different wavelengths with each experiencing a different birefringence in the same optical fiber. Therefore, many different group delays occur in the same pulse and as it propagates the optical fiber a broadening is observed. For this reason, it is more meaningful to discuss the average DGD for a given wavelength range,

this quantity is referred to as polarization mode dispersion (PMD). In short optical fiber lengths PMD behaves in a linear fashion so is measured in ps/km. PMD is an important quantity in communications because pulse broadening and random-walk can lead to an increase in bit error rate (BER) and an overall decrease in system performance.

Due to inconsistencies in optical fiber density and stress, birefringence varies randomly within an optical fiber. This makes a lightwave's SOP vary randomly as it propagates the optical fiber. Surprisingly, two orthogonal PSP still exist (Buck, 1995). However, the PSP are no longer necessarily linear polarized states and are only invariant to frequency to first order. Their invariance to frequency makes the two PSP the optimal polarization condition for launching pulses in long communication systems because different wavelengths do not experience PMD. Regardless of intrinsic birefringence variation, PMD is not a major limitation to low-speed communication systems or in short optical fiber lengths. However, in long, high-speed communication systems, PMD can lead to detrimental system errors. This will be discussed later in the text.

Under normal conditions, communication SMF does not have any significant preference for specific transmitted SOP. However, optical fiber splices and microbends can lead to preferential polarization transmittance. The optical fiber can act as a partial polarizer resulting in certain SOP being transmitted more than others, an effect called polarization dependent loss (PDL). PDL in dB is defined as:

$$\text{PDL} = 10\log\left(\frac{T_{max}}{T_{min}}\right), \tag{2.7}$$

where T_{max} is the maximum transmitted intensity and T_{min} is the minimum transmitted intensity with respect to all SOP. Polarization dependent components are the greatest contributor to PDL in communications. PDL is generally more significant in longer communication systems.

The basics of birefringence, PMD, and PDL in optical fiber have now been reviewed. This discussion only considered time invariant birefringence. In short optical fiber lengths this description is often adequate because of the minimal environmental exposure to the optical fiber. However, in the long optical fiber regime, a far more developed discussion with new parameters must be realized.

2.3 Polarization Evolution in Long Optical Fiber

In long optical fiber and long optical fiber communication systems, SOP evolution becomes very complex due to randomly varying birefringence, misaligned splices, optical fiber bends and stresses, and even different types of optical fiber spliced into the system. While the progression of SOP is complicated, none of these features are time-variant and at a given wavelength and input SOP the output SOP would be constant. Such an optical fiber can easily be characterized and modeled.

In the linear regime, PMD adds proportional to the length. However, in longer optical fibers, because of the random changes to the birefringence, the accumulation of PMD becomes proportional to the square root of the distance (Kaminow, 1997). In other words, a long optical fiber link experiences a lower dispersion than expected from the synergy of its linear PMD sections. This feature of long optical fiber allows for extremely long haul optical communication systems.

In long optical communication systems, the environmental exposure is much greater than in shorter optical communication systems. When analyzing any long optical fiber link, the output SOP randomly experiences drift. The SOP decorrelates over time, eventually covering the entire surface of the Poincare sphere. The random SOP changes are caused by random ambient temperature changes, thermal gradients, bending caused by wind or ocean

currents, and electromagnetic fields. When considering time varying SOP changes, the previous static model of optical fiber characterization is not useful. The only useful means of analysis is statistical methods.

The correlation length is a parameter that can be used to determine if a communication system is going to experience SOP decorrelation. The correlation length is defined as (Kaminow 1997):

$$\frac{\langle P_{\parallel}(l_c)\rangle - \langle P_{\perp}(l_c)\rangle}{P_{total}} = \frac{1}{e^2}, \tag{2.8}$$

where l_c is the correlation length, $P_{\parallel}$ is the optical power in the original polarization mode, $P_{\perp}$ is the optical power in the orthogonal polarization mode, $\langle ... \rangle$ is the average over all fiber lengths, and P_{total} is the total optical power. The model is convenient because it considers only the accumulation of SOP modulating effects. If the length of the optical fiber is $\ll l_c$ the optical fiber is still in the linear PMD regime, and if the optical fiber length is $\gg l_c$ the optical fiber is in the nonlinear regime and statistics should be used. The SOP evolution of an optical fiber in both the linear and nonlinear PMD regimes is shown in figure 2.4.

In an optical communication system where the length is $\gg l_c$ the distribution of PMD measured over a long time interval gives the most useful determination of the systems performance. An analysis of the PMD distribution shows whether the system is performing to its specifications or if it can be upgraded to a higher-speed network. It may be determined that environmental factors are simply too intense and fast to be dynamically PMD compensated.

PMD and PDL generally coexist in long communication systems. The combination of these two polarization dependent effects makes the SOP evolution very complex. The existence of PDL can increase DGD and the existence of PMD can result in wavelength dependent PDL (Damask, 2004). While PMD depolarizes the lightwave, PDL competes to

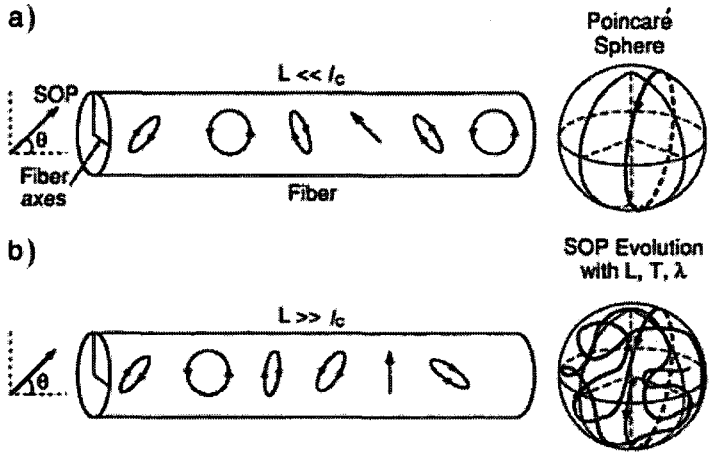

Figure 2.4 An example of the SOP evolution through an optical fiber when a) the optical fiber length is much shorter than the correlation length and when b) the optical fiber length is much longer than the correlation length (from Kaminow, 1997)

repolarize the lightwave. For these reasons, among others, modern communication system models consider both PMD and PDL. Long optical fiber links often contain amplifiers; it is important to mention that amplifiers can introduce polarization dependent gain (PDG), the complement of PDL. PDG may also be a significant contributing factor to the SOP evolution in communication systems.

Chapter 3

Optical Fiber Current Sensing

3.1 The Present State of Optical Fiber Current Sensors

Optical fiber current sensors (OFCS) employ the following magneto-optic effects: the Voigt effect, the Cotton-Mouton effect, the magneto-optic Kerr effect, or the Faraday effect. The Voigt effect and Cotton-Mouton effect are second-order linear birefringent effects generated by a perpendicular magnetic field; however, they are both insignificant in optical fiber at the communication wavelength, $1550\ nm$. The magneto-optic Kerr effect is a first-order polarization effect that results when a linear polarized light reflects off a magnetic surface. The Faraday effect is a first-order circular birefringent effect generated when a longitudinal magnetic field is applied. This effect can be significant in optical fiber at $1550\ nm$.

The Faraday effect is observed as a rotation of the plane of polarization. The expression for the magnitude of Faraday rotation in radians is:

$$\theta = v \int B \cdot dl, \tag{3.1}$$

where v is the Verdet constant, B is the magnitude of the magnetic field applied in the parallel direction, and l is the length over which the field and light interact.

Despite its name, the Verdet constant is actually a function of frequency and temperature, $v(f, T)$. v is proportional to the square of the frequency. The Verdet constant for silica glasses in the telecom wavelength range of $1520\ nm - 1565\ nm$ is $v = (0.142 \times 10^{-28} \pm 0.002) f^2$ (Prat, 1999). This translates to a low value of$0.53\ rad/(m \cdot T)$ at $1550\ nm$. The typical temperature dependence is silica fiber is $1/v \cdot \mathrm{d}v/\mathrm{d}T = 6.9 \pm 0.3 \times 10^{-5}/^{\circ}$ (Williams, 1991). As a result the ambient temperature dependency of the Faraday effect is very small.

The relation in equation 3.1 holds exactly for the ideal case when linear birefringence is negligible in the medium. When a constant linear birefringence exists in the medium, however, the v must be calculated as a function of the induced birefringence. Linear retardance usually dominates the temperature effect and must be avoided for an accurate OFCS.

Many OFCS sensors are fabricated with special magneto-strictive coated optical fibers to obtain high sensitivity in short lengths of optical fiber. However, an OFCS that employs only regular SMF is cost-effective and simple to implement. OFCS are of interest because they benefit from extremely fast response times and very low magnetic permeability. Using a magneto-strictive coating can limit the response time (Lenz, 2006), the range of current detection due to magnetic saturation (Wang 2008), and in some cases, can affect the sensors magnetic permeability (Ekreem 2007). However, they are invaluable for their very low current detection and size.

Currently, the power industry is dominated by polarization rotation sensors (Miguel, 2002). However, there are many current sensors that rely on similar designs to an optical fiber gyroscope, called the Sagnac loop interferometer. This interferometer has an advantage of detecting small phase change, because it detects derivative phase change, rather than the phase change itself, as is the case with the Mach-Zehnder and Michelson interferometer. For this type of OFCS, the dominant magneto-optic effect is the Faraday effect. Essentially, a current-induced non-reciprocal phase modulation occurs due to the induced circular birefringence. The quantity of the phase delay between the circular polarization components is then equal to twice the polarization rotation angle shown in equation 3.1 (Grattan, 2000). This phase modulation is detected by the Sagnac loop interferometer as a change in the intensity of the optical output signal.

Due to the non-reciprocal nature of the Faraday effect, many OFCS sensors use Faraday rotation mirrors (FRM). The FRM is composed of a permanent magnetic, that rotates the plane of polarization 45^o using the Faraday effect, and a mirror to backreflect the light signal. After reflection, the light is then rotated a non-reciprocal 45^o by the permanent magnet and the exiting light beam is orthogonally polarized to the incoming lightwave. As discussed in section 2.2, when an orthogonally polarized lightwave travels through a reciprocal birefringence, i.e., temperature gradient, vibration, etc., the polarization modulation will be removed. When the FRM is used in the presence of a non-reciprocal birefringence, i.e., Faraday effect, the polarization modulation will be doubled. As shown in equation 2.6, in the presence of a non-reciprocal birefringence, linear birefringence becomes non-reciprocal. Also, for a polarization rotation sensor, this means linear birefringence quenches the current induced polarization rotation (Cruz, 1996). In contrast, for an interferometric sensor, linear birefringence increases the current induced phase change (Blake, 1996). In both cases, this linear birefringence leads to instability in OFCS. This will be discussed later in this chapter.

3.2 The FRM Cavity Sagnac Loop Interferometric OFCS

A novel sensitive magneto-optical OFCS is designed using a Sagnac loop interferometer and an optical fiber cavity formed with a coupler and two FRM. The Sagnac loop configuration was chosen for its high sensitivity and potential for high-frequency response (Udd, 1990). The two FRM are employed to decrease the length of the fiber under test (FUT) while still maintaining the effective length of the sensor and an insensitivity to linear birefringence effects (Sabert, 1994). This sensor is very easy to construct and is made from standard communication system devices.

The experimental setup uses a broadband light source centered around 1550 nm. The short coherence length of the broad source reduces coherence noise from the optical fiber-delay line and FRM cavity. Also, it greatly reduces the cost of the sensor by not using a laser source. A C-band erbium doped fiber amplifier (EDFA) amplifies the broadband light source to meet the minimum input power requirement for the sensor system. The light signal is then passed through a linear polarizer. This is an important step because only a small portion of the light emitted from the broadband light source is polarized. The input SOP is optimized using a polarization controller, PC1. This is required because the output sensitivity is input SOP-dependent. The light passes through a circulator which allows for detection of the returning orthogonal output signal for differential detection (Wang 2008) from the Sagnac loop. It also provides isolation of the source from returning light. The light enters the Sagnac loop through a 3 dB coupler. A 3 dB coupling ratio is the optimal condition for a Sagnac loop interferometer (Jang, 2002). A polarization controller, PC2, is added inside the Sagnac loop to satisfy the quadrature condition by controlling the birefringence in the loop (Jang, 2002) and maximizing the output sensitivity. On the adjacent side of the loop, an optical fiber-delay line is added to create a phase delay between the CW and CCW waves. Both lightwaves are then recombined via a 3 dB coupler. The lightwave then enters another coupler, which forms a cavity with SMF-28 and two FRM (FRM1 and FRM2). This coupler controls the percent of light kept inside the cavity. A higher coupling ratio ensures multiple passes within the FRM cavity. An FRM has two main advantages over a conventional mirror: it minimizes the effects of linear birefringence in the FUT and it keeps the recombining light from FRM2 the same SOP as the light being input into the cavity. These features help to ensure cavity stability. When the light returns, it interferes as it leaves the Sagnac loop. The output signal is then detected by an avalanche photodiode (APD) (light

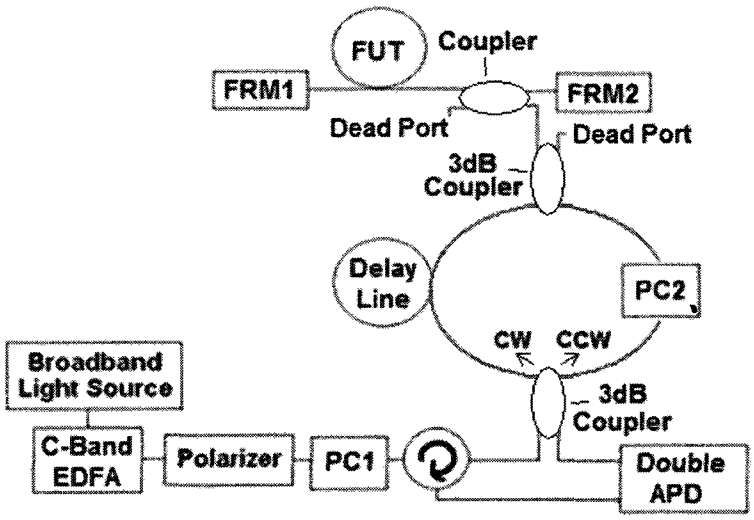

Figure 3.1 The experimental test setup for the FRM cavity Sagnac loop interferometric OFCS with differential detection.

port) and the orthogonal output travels through a circulator and is detected by another APD (dark port). The electrical signals are then recorded using an oscilloscope data acquisition (DAQ) card. The experimental setup is shown in figure 3.1.

Experiment

To generate a constant magnetic field in the direction of the light propagation, the optical fiber spool is wrapped with wire, forming a surrounding toroidal coil. The method is visualized in figure 3.2. This method is more convenient than using a single wire because a large magnetomotive force can be generated with low currents inside the toroid, while no magnetic field is generated outside the structure. To generate the magnetomotive forces used

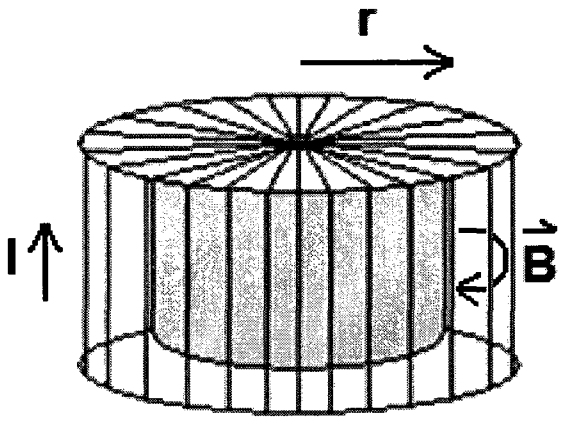

Figure 3.2 A toroidal coil formed by wrapping wire around a spool of optical fiber.

in these experiments, the optical fiber spool was wrapped with $N = 20\ t$, where N represents the number of turns of wire, and $r = 0.0425\ m$, where the r is the radius of the optical fiber.

Detection

For the case of a single FRM (double pass), the expression for the magnetomotive force induced phase modulation at frequency ω_C, is $\phi_C(t) = \Phi\cos(\omega_C t)$, where $\Phi = 4\kappa INL$ and $\kappa = vB/(I \cdot N)$. If the ideal $3\ dB$ coupling ratio is met at the optical fiber input, the output interference equation for the two detectors is then expressed as (see Appendix):

$$I = \frac{\alpha I_o}{4}\left\{1 \pm \frac{1}{2}\cos\left(\phi_b + 2\,\Phi\sin\left\{\omega_C\left(t - \frac{\tau_{tot}}{2}\right)\right\}\sin\left\{\omega_C\frac{L_d n}{2c}\right\}\right)\right\}, \quad (3.2)$$

where α is the loss of the system, I_o is the intensity of the light source at the input optical fiber, L_d is the length of the optical fiber-delay line, n is the refractive index of the optical fiber core, c is the speed of light in free space, and τ_{tot} is the total time for the CW or CCW beams to travel the optical path of the interferometer.

One important feature of equation 3.2 is that the Sagnac loop is most sensitive to one specific frequency. This frequency is determined by the length of the optical fiber-delay line. From equation 3.2, the condition for the optimal optical fiber-delay line length is $\omega_C L_d n/c = \pi$. This expression also makes the Sagnac loop interferometer a better sensor for detecting higher frequencies because low frequency measurement requires very long optical fiber-delay lengths. The high cut-off frequency for the available programmable power supply generating the current was $50\ kHz$. For this reason, experiments with $2\ km$ ($50\ kHz$) and $10\ km$ ($10\ kHz$) delay lines are performed. It is important to realize that this sensor may be capable of detecting MHz or possible GHz at a similar sensitivity with a short delay line and the correct high-speed detectors and DAQ card.

If $\omega_C L_d n/c = \pi$, PC2 is adjusted to quadrature, $\phi_b = \pi/2$, and the applied magnetomotive force is low such that $\Phi \ll 1$, then using the small angle approximation, equation 3.2 becomes (see Appendix)[1]:

$$I \cong \frac{\alpha I_o}{4}\left\{1 \mp 2\Phi \sin\left\{\omega_C\left(t - \frac{\tau_{tot}}{2}\right)\right\}\right\}, \qquad (3.3)$$

The equation shows that the AC component of the interference intensity, for both channels, is proportional to the phase change from the magnetomotive force.

When the light undergoes multiple passes in the FRM cavity, caused by an increase in coupling ratio, the detected intensity is the summation of the AC intensities, $I_1(\Phi_1) + I_2(\Phi_2) + \ldots$, where $\Phi_1 = 4\kappa INL$, $\Phi_2 = 8\kappa INL$, etc.. This will effectively increase the sensor response and improve the SNR of the system, while maintaining linearity to the applied current. The lossy nature of the cavity is the greatest limitation to the SNR improvement.

[1] Small errors in the assumptions exist because a broadband source is used. Here chromatic dispersion in the delay line and the wavelength dependence of the polarization controller are assumed to have a minimal influence on the visibility and will be neglected in this derivation.

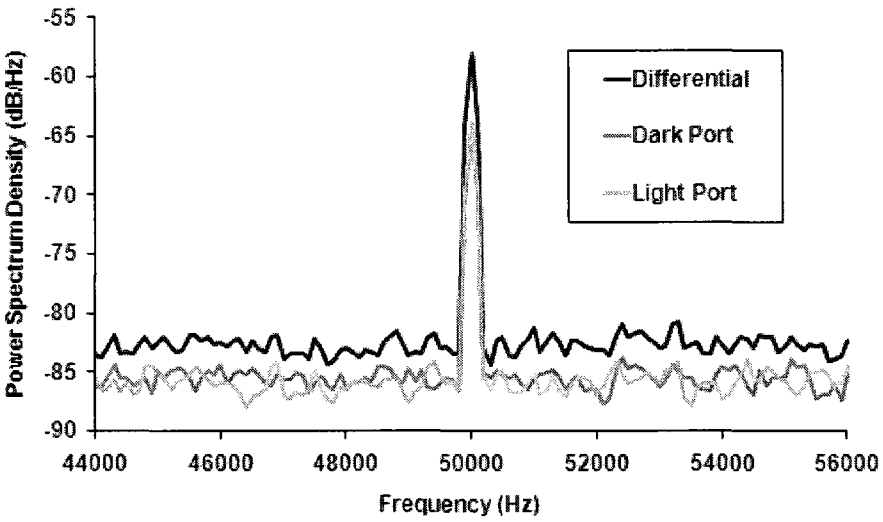

Figure 3.3 An example of the PSD for both the differential signal, the dark APD port, and the light APD port signal.

The data was collected at the dark port and light port at $5\ Msamples/s$ for $1.5\ Msamples$ when using the $2\ km$ delay line and $3\ Msamples/s$ for $1.2\ Msamples$ when using the $10\ km$ delay line with the DAQ card (NI-5112). When the two detected APD signals are recorded they are subtracted via a software subtraction. This minimizes the DC signal and common noise in both channels and constructively adds the AC signals improving the sensitivity. An example of the power spectrum density (PSD) for both APD channels and the differential signal after the software subtraction are shown in figure 3.3. All power spectrum density data is averaged 30 times to get a good estimation of the true noise floor of the system. The SNR gain from the differential detection scheme is ~3 dB.

To optimize output sensitivity, the coupling ratio in the FRM cavity should be raised to increase the effective length of the sensor. To observe the influence of coupling ratio on the SNR, measurements were done with the following coupling ratios: $0\ dB$, $3\ dB$, and

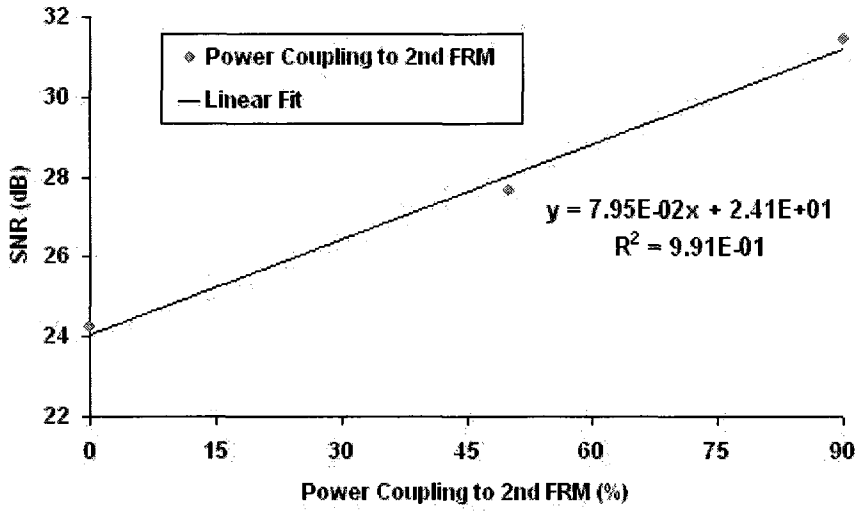

Figure 3.4 The measured SNR vs. power coupling to FRM2 at the peak frequency sensitivity, $50\ kHz$, for an $100\ m$ FRM cavity.

$10\ dB$. Figure 3.4 shows the measured SNR vs. power coupling to FRM2 for a $50\ kHz$ current, $100\ m$ FUT, and a $2\ km$ delay line. A positive linear relation between the SNR (dB) and the power coupling to FRM2 is observed. This suggests that increasing the coupling ratio would always improve the systems SNR. However, there exists a limitation to increasing the coupling ratio further due to the power penalty imposed to the system.

A major issue for the low-frequency Sagnac loop interferometric sensor is Rayleigh backscatter noise. As mentioned, the delay line length must be a very long to detect low frequencies. The increase in optical fiber length results in higher Rayleigh backscatter noise. The broadband light source has been implemented to minimize coherent backscatter noise. In figure 3.5, the detection of a $10\ kHz$ current, a $2\ km$ delay line, and an $100\ m$, $3\ dB$ FRM cavity is shown. The large noise shoulder created from backscatter noise will be convoluted with any signal lower than $10\ kHz$. From this measurement it can be concluded that the short coherence length of the source does not compensate completely for the backscatter noise.

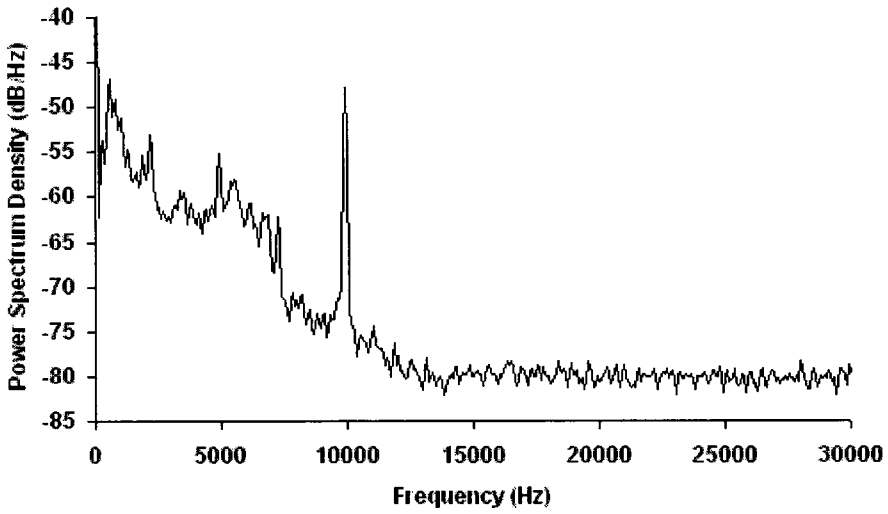

Figure 3.5 The differential PSD at the peak frequency sensitivity, $10\ kHz$, for an $100\ m$, $3\ dB$ FRM cavity.

Another technique to remove the Rayleigh backscatter noise from a Sagnac loop interferometer is sideband modulation of the source (Chow, 2007). This technique requires phase modulator to generate sidebands to the input spectrum and an additional Mach-Zehnder interferometer before the Sagnac loop. If the modulation frequency is chosen to be half the free spectral range of the Mach-Zehnder interferometer then the Sagnac loop CW is composed of only the sideband frequencies and the CCW is composed of only the carrier frequency. The output coupler will then act as a dual tap filter, with one output port containing the backscatter noise and the other the Sagnac loop signal. Our system has a rather strict power requirement, due to the many couplers and the polarization filtered low DOP source, the delay line should not be excessively long because of the increased loss. Therefore, no low-frequency detection scheme is used.

The sensor output can also be analyzed in the time domain. A typical differential time domain plot is shown in figure 3.6 a) for the $100\ m$, $10\ dB$ FRM cavity with a

$357.25\ A_{rms} \cdot t$ magnetomotive force applied, where A_{rms} represents amperes root mean square. Due to the strong presence of low-frequency Rayleigh backscatter noise, the magnetomotive force induced phase modulation is not obvious in the time domain signal. To analyze the $50\ kHz$ signal in the time domain, a second order butterworth software bandpass

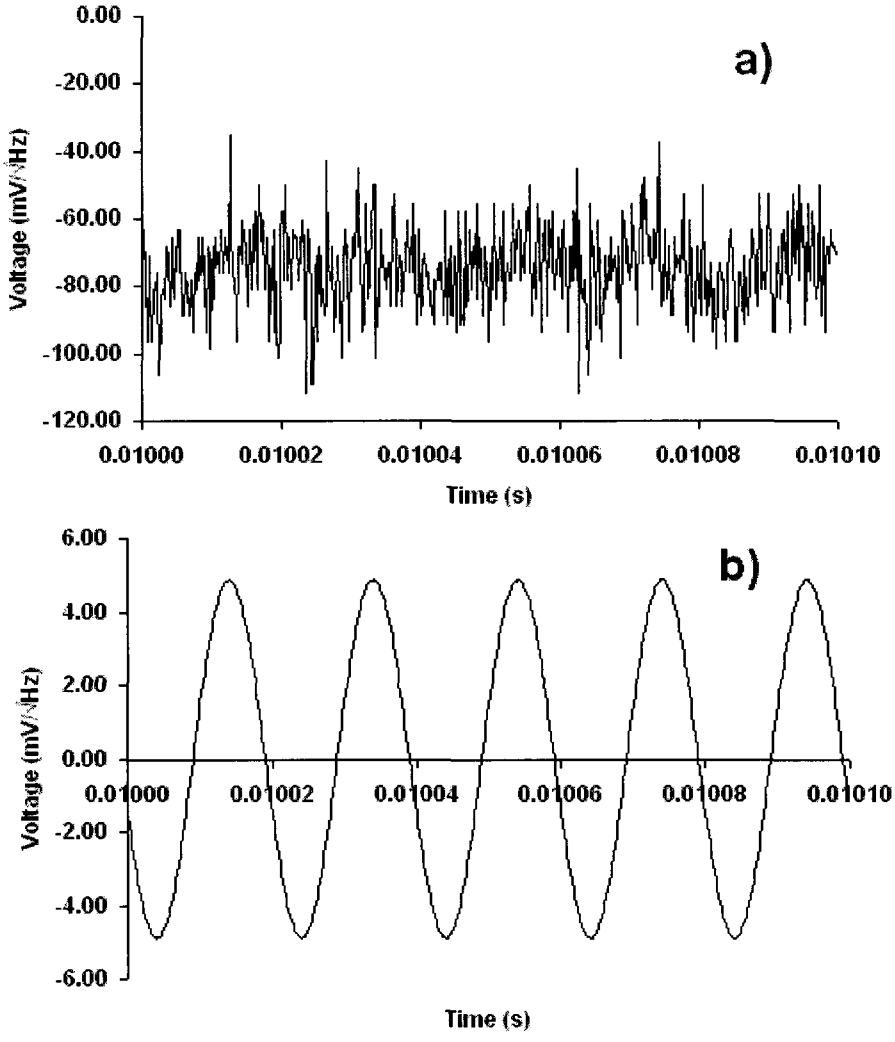

Figure 3.6 A sample of the a) differential time domain signal and the b) bandpass filtered $(49.8\ kHz - 50.2\ kHz)$ differential time domain signal for a measurement of $50\ kHz$, $357.25\ A_{rms} \cdot t$ magnetomotive force using an $100\ m$, $10\ dB$ FRM cavity.

filter ($49.8\ kHz - 50.2\ kHz$) is applied to the previous data. The filter result is shown in figure 3.6 b). Here the $50\ kHz$ time domain signal is resolved from the noise background. From this analysis it can be concluded that to observe the signal frequency in the time domain, an electrical filter or software filter should always be applied. It is important to note this filter cannot resolve low-frequency signals from the Rayleigh backscatter noise.

3.3 Performance of the FRM Cavity Sagnac Loop Interferometric OFCS

System Response and Resolution

The measured system response as a function of the applied magnetomotive force is shown in figure 3.7. A linear least squares fit of the data shows the system response is very linear for low magnetomotive forces. The slope of the linear fit is $6.2376 \times 10^{-3}\ mV_{rms}/\left(A_{rms} \cdot t \cdot \sqrt{Hz}\right)$. The minimum detectable magnetomotive force is determined by the systems resolution. To find the system resolution, a background power spectrum density measurement is used to estimate the noise floor at $50\ kHz$, this data is shown in figure 3.8. The noise power spectrum density at $50\ kHz$ is $-83.537\ dB/Hz$ or the equivalent $0.066551\ mV_{rms}/\sqrt{Hz}$, which corresponds to a minimum detectable force of $10.669 A_{rms} \cdot t/\sqrt{Hz}$. Using that the toroid had $20\ t$, the minimum detectable current in this experiment is $0.53345\ A_{rms}/\sqrt{Hz}$. The maximum response of the sensor was not measured.

The measured system resolution is comparable to the Sagnac loop interferometric OFCS that uses a Rogowski coil and a piezoelectric transducer (PZT) (Wang, 2001). It also has better sensitivity than a conventional reciprocal reflection interferometer with twisted SMF at $1330\ nm$ (Lin, 1999). Typically, OFCS using magnetostrictive coated optical fiber have a much higher resolution than reported here (Wang, 2008). However, neither the magneto-strictive nor the Rogowski coil and PZT have a high-frequency response, a key

feature of the reported sensor is its potential for very high-frequency response. The system resolution is very high considering no Rogowski coil and PZT, magneto-strictive coating,

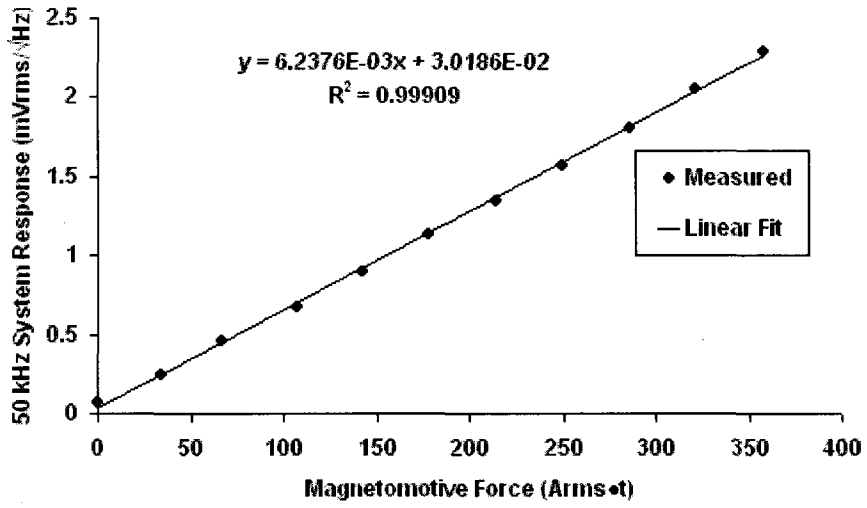

Figure 3.7 The measured $50\,kHz$ system response vs. magnetomotive force for an $100\,m$, $10\,dB$ FRM cavity.

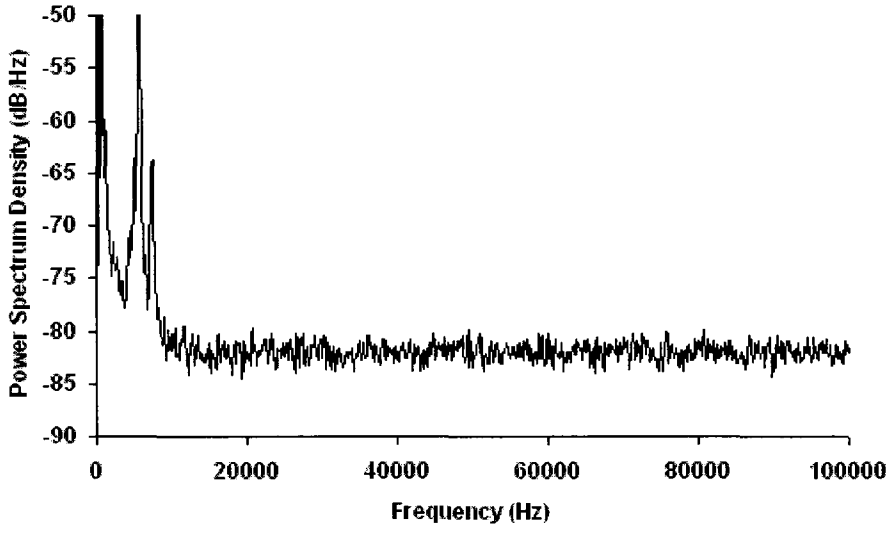

Figure 3.8 The background power spectrum density for an $100\,m$, $10\,dB$ FRM cavity.

annealed twisted optical fiber, or high birefringence optical fiber is used. Examples of sensitive high-frequency current sensor applications include: medical applications, such as diathermy and high-frequency magnetic resonance imaging, and power industry applications, such as high power inductors and high frequency power transformers.

The input SOP dependence is shown in figure 3.9. A least squares fit reveals a slope of $9.30 \times 10^{-3}\ dB/number\ of\ random\ polarization$. Due to the low slope, the coefficient of variation is very sensitive and it is more informative to analyze the standard deviation of the data. The standard deviation is $0.271\ dB$, or $0.882\ \%$ the mean value. From this result it can be concluded that the input SOP has only a small affect on the system resolution. However, the variation is significant enough a polarization controller should be included to maximize the system resolution. The other SOP dependence comes from the variation of PC2 inside the Sagnac loop. In fact, if PC2 is varied to find the poorest system resolution the SNR will go to $0\ dB$. Therefore, it is very important that the ideal SOP should

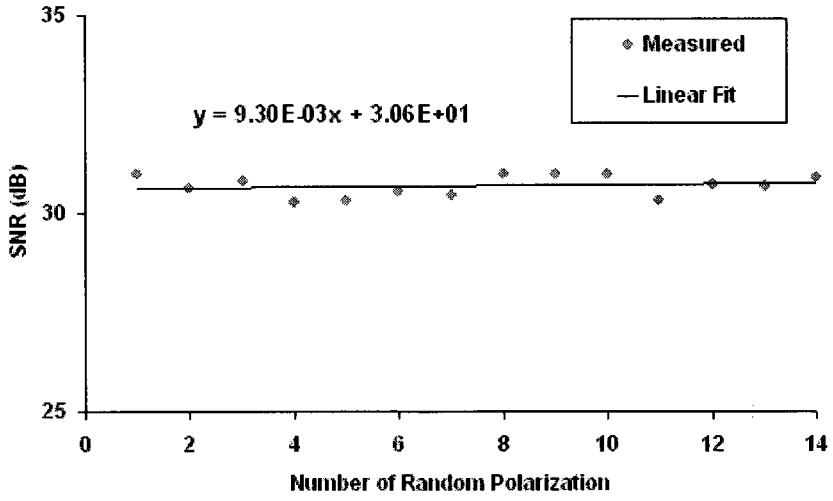

Figure 3.9 The measured SNR variation for different input SOP of an $100\ m$, $10\ dB$ FRM cavity with a $50\ kHz$ magnetomotive force of $357.25\ A_{rms} \cdot t$.

be found to maximize the system resolution.

Optical Spectrum Narrowing

An optical cavity is formed using two highly reflective surfaces. Upon multiple reflections, the effects of interference will favour certain longitudinal modes. These modes will depend on the length of the cavity and be the resonant (dominant) frequencies in the optical spectrum. The FRM cavity is similar in many ways to an extended optical cavity because it contains an optical wave and two reflective surfaces. However, due to the short coherence length of the broadband source, $L_{coherence} \ll L_{cavity}$, no interference will be observed. The FRM cavity spectrum should still favour a resonance wavelength due to the wavelength dependent attenuation of the FRM. The wavelength dependent attenuation for the FRM is $\sim 0.1\ dB$ across the spectrum of the broadband source. Upon multiple reflections the spectrum is expected to narrow for higher coupling ratios because the attenuation of certain wavelengths is higher.

To observe this feature the optical spectrum from a broadband source, C-band EDFA, polarizer, circulator, and FRM cavities of different coupling ratios are measured with an optical spectrum analyzer (OSA). The EDFA was set to a constant current for all tests. This

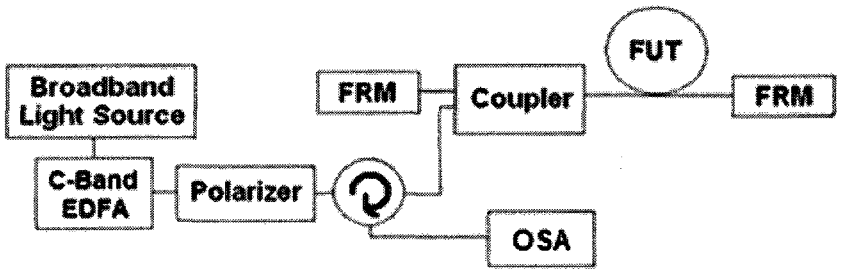

Figure 3.10 The setup for measuring spectral narrowing as a function of coupling ratio in the FRM cavity.

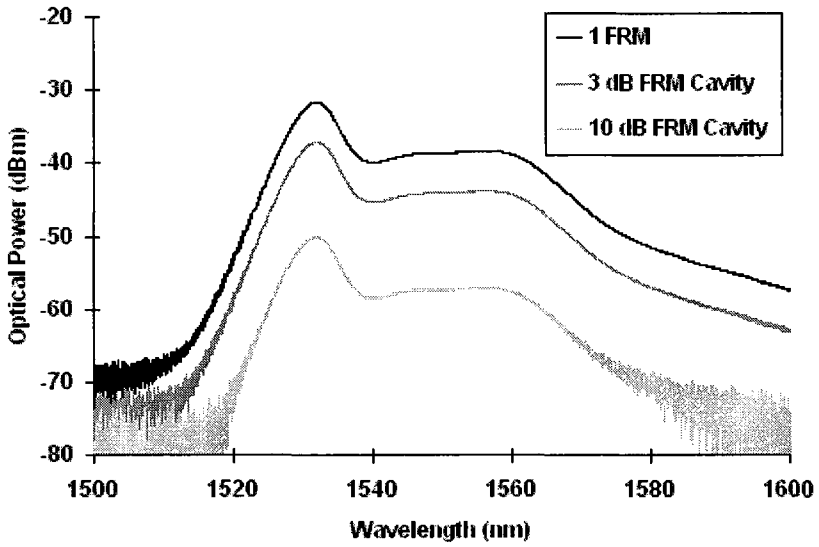

Figure 3.11 The measured optical spectra of the broadband source for the three different FRM cavity coupling ratios and an $100\ m$ FUT.

ensures that the profile of the emission spectrum did not change because of the EDFA. The setup is shown in figure 3.10.

The optical spectrum for the single FRM, the $3\ dB$ FRM cavity, and the $10\ dB$ FRM cavity with an $100\ m$ FUT are shown in figure 3.11. A measurement of the full width at half maximum (FWHM) and the $-10\ dB$ width can be used to determine if spectral narrowing occurs. At the FWHM no narrowing is observed beyond the large uncertainty of the OSA, $\pm\ 0.06\ nm$. At the $-10\ dB$ width the narrowing for the $3\ dB$ FRM cavity is $0.07\ nm$ and for the $10\ dB$ FRM cavity it is $0.52\ nm$. The narrowing cannot be observed at the FWHM because only a small change in the optical spectrum is expected. At the $-10\ dB$ width a small change to the optical spectrum is much more visible because a low power fluctuation will have a greater influence. The spectral narrowing at the FWHM could be measured with

a more accurate OSA. The realization of spectral narrowing with the increase of coupling ratio indicates the presence of a resonant wavelength in the FRM cavity.

Temperature Stability

Ambient temperature changes do not have a major influence on sensor stability due to the low temperature dependence of the Verdet constant. However, surface heating-induced temperature gradients may affect measurement reliability. For this reason, temperature stability is a major issue in the OFCS. Many features in the design of the FRM cavity Sagnac loop interferometric OFCS are used to mitigate the sensor's temperature dependency. Importantly, the sensing optical fiber is separated from the Sagnac loop so the delay line and polarization controller can easily be shielded from temperature changes. Also, the FRM cavity has an FRM in both arms of the coupler to reduce the sensor's dependency on linear birefringence.

To test the temperature stability, one side of the optical fiber spool containing the FUT was heated with a $60\ watt$ light bulb for a $10\ minute$ period. The temperatures of the surfaces of four sides of the optical fiber spool were monitored with four omega high-precision thermistor probes (Omega 300 Series Banjo Style). A $50\ kHz$ magnetomotive force of $357.25\ A_{rms} \cdot t$ was applied to the FUT during the period. The temperature data and results of the test are shown for the $100\ m$, $10\ dB$ FRM cavity in figure 3.12. Linear least squares fits of the system response and SNR data shows very good stability when the irradiated side was heated $6.35°C$ over a 10 minute period. The change in the system response and SNR observed was only $-1.1401 \times 10^{-4}\ mV_{rms}/(\sqrt{Hz} \cdot s)$ and $-4.14 \times 10^{-4}\ dB/s$, respectively. Using the slope parameter from the linear fit in figure 3.7 and the noise floor measurement from figure 3.8, an uncertainty of $\pm 10.967\ A_{rms} \cdot t/(\sqrt{Hz})$ in the

measured magnetomotive force and an increase of $0.395\ A_{rms} \cdot t/\sqrt{Hz}$ in the minimum detected magnetomotive force for a heating of this type is found. From this result it can be concluded that in the presence of small temperature gradients the sensor's temperature

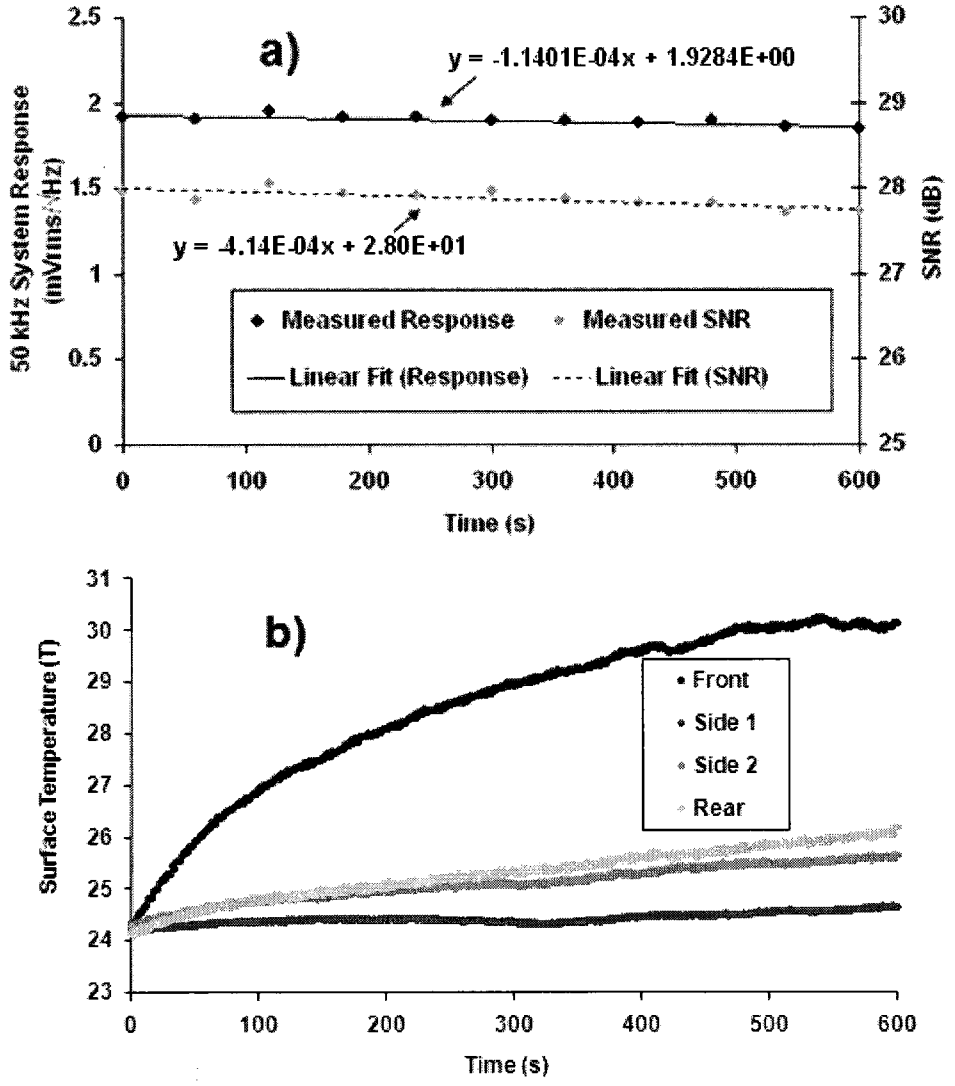

Figure 3.12 a) The measured system response and SNR of an $100\ m$, $10\ dB$ FRM cavity with a $50\ kHz$ magnetomotive force of $357.25\ A_{rms} \cdot t$ and b) the surface temperature measurements during heating of one side of the optical fiber spool with a $60\ watt$ light bulb.

dependence is similar to the minimum system response when measuring low magnetomotive forces.

3.4 Quenching of Faraday Effect in Long Optical Fiber

In long optical fiber, the output polarization is highly dependent upon the PMD and PDL in the optical fiber length. This makes it very difficult to quantify the Faraday rotation in a long optical fiber due to perturbations. To determine the maximum DC Faraday rotation angle in long optical fiber, a method developed by Brodsky et. al (Brodsky, 2005) can be used. In their study, the maximum Faraday rotation angle was determined with a polarization scrambler and a FRM. The angle is also linearly proportional to magnetic field. Here this method will be explored and used to show the existence of quenching of the Faraday effect in long optical fiber. While linear birefringence is known to quench the Faraday effect in short optical fiber lengths (Miguel, 2002), this behaviour has not been shown in long optical fiber lengths.

The setup includes two polarization controllers, one at the optical fiber input (PC1) and one polarization controller (PC2) on scramble mode inside the FUT ($10\ km$, SMF-28). The FUT is then terminated by an FRM and the backreflected signal is sent through a circulator to a polarization analyzer (Agilent 8509B) and recorded. The experimental setup is shown in figure 3.13. During a measurement when no magnetic field is present on the FUT, the FRM can cancel the polarization scrambling completely. When a DC magnetic field is applied, however, the FRM cannot completely cancel the polarization changes induced by the scrambler. This occurs because the reciprocal linear birefringence becomes non-reciprocal in the presence of the Faraday effect, see section 3.1.

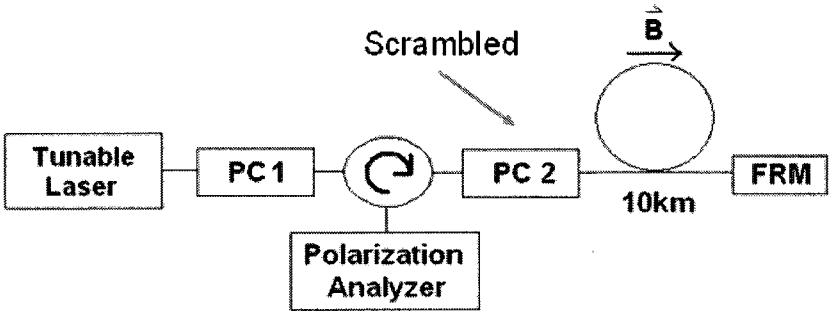

Figure 3.13 The setup for measuring the maximum Faraday rotation angle for a given FUT and input SOP.

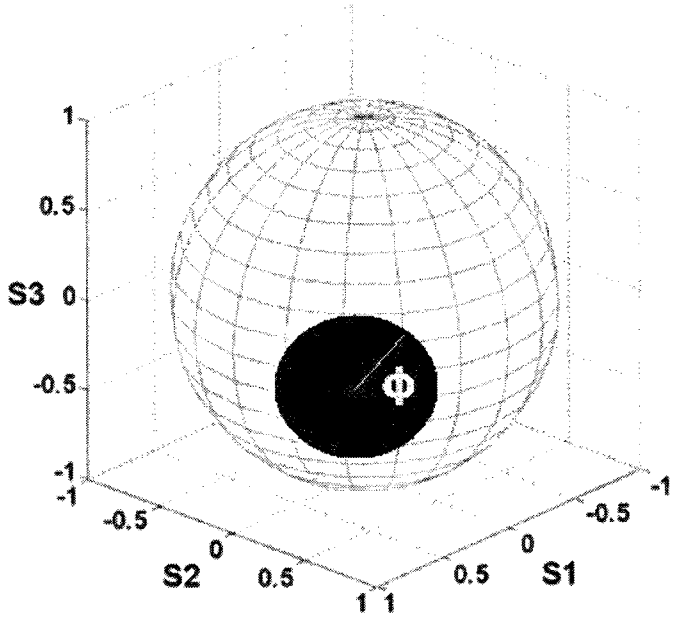

Figure 3.14 An artistic rendition of the plot on the Poincare sphere and an arc length, ϕ, representing the maximum Faraday rotation angle.

Due to the large amount of data recorded for the measurement, a 3D plot could not be generated showing the "cap" that is generated on the surface of the Poincare sphere during the experiment. An artistic rendition of the plot on the Poincare sphere and the arc length, ϕ,

is shown in figure 3.14. This can easily be observed on the output plot of the Agilent 8509B polarization analyzer software. The maximum Faraday rotation angle is defined as the arc length in radians and is calculated using the following definition:

$$\phi = \cos^{-1}[\overrightarrow{S_1} \cdot \overrightarrow{S_2}], \tag{3.4}$$

where $\overrightarrow{S_1}$ is the normalized Stokes vector terminating at the center of the cap and $\overrightarrow{S_2}$ is normalized Stokes vector terminating at the edge of the cap. The cap is assumed to have a circular base because a calculation using any edge point yields very similar values of ϕ.

To observe the input SOP dependence of the maximum Faraday rotation angle, PC1 was varied via general purpose interface bus. The input SOP dependence of the maximum Faraday rotation angle at a constant current is shown in figure 3.15. A linear least squares fit of the data finds a slope of -6.23×10^{-5} $rad/number\ of\ random\ polarization$. Due to the low slope, the coefficient of variation is very sensitive and it is more informative to

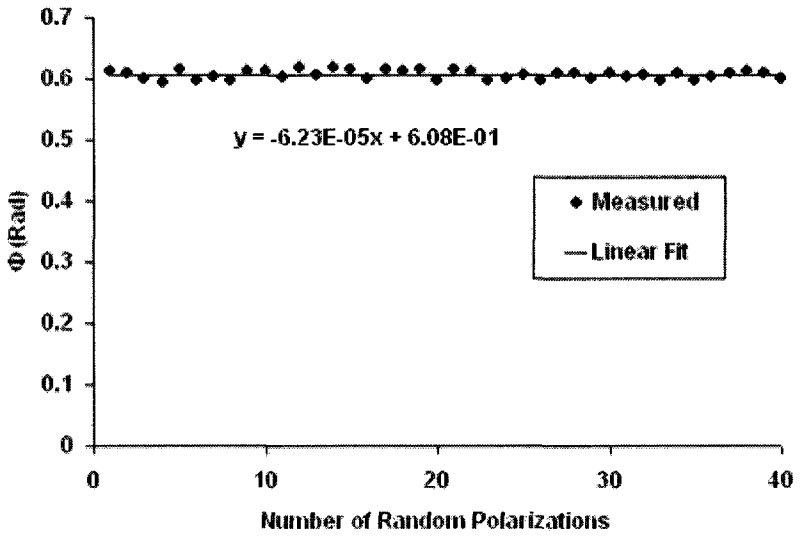

Figure 3.15 The measured maximum Faraday rotation angle at a constant current for 40 different input SOP in a 10 km length of optical fiber.

analyze the standard deviation of the data. The standard deviation is $7.04 \times 10^{-3}\ rad$, or 1.16 % the mean value. The data shows that, regardless of the input SOP, ϕ is constant. This result is important because any instability in the sources SOP or between the source and the circulator will not affect the maximum Faraday rotation angle and the DC current can be determined.

This method could be used for DC magnetic field sensing with the advantage of no input polarization dependence. Due to the dependence of linear birefringence in the FUT, however, the maximum Faraday rotation angle may still be unstable with time.

To observe the behavior of the maximum Faraday rotation angle with changing linear birefringence, heat was applied to the $10\ km$ optical fiber spool. A $60\ watt$ light bulb was used to heat the surface of one side of the optical fiber spool, inducing a temperature gradient in the FUT. The SOP was then recorded for an 800 s time interval for a constant-input SOP. No temperature readings were recorded because it would be very difficult to quantify the temperature gradient over such a long length of optical fiber. The measured maximum Faraday rotation angle at a constant current and a constant input is shown in figure 3.16. A linear least squares fit[2] of the data shows a strong linear fit and has a slope of $-1.39 \times 10^{-4}\ rad/s$. In the 10-minute time period this results in a change of $-0.111\ rad$, or a -17.9 % change in ϕ. The result shows that a quenching of the maximum Faraday rotation angle is observed. This result is important because higher birefringent optical fibers may not be as vulnerable to SOP changes caused by an external magnetic field. Two particularly important situations where higher birefringent optical fibers are needed are: optical ground

[2] A linear fit is shown to be valid for small temperature gradients applied for short time periods, as used in this analysis. However, when considering large temperature gradients and long time periods, high-order approximations are required.

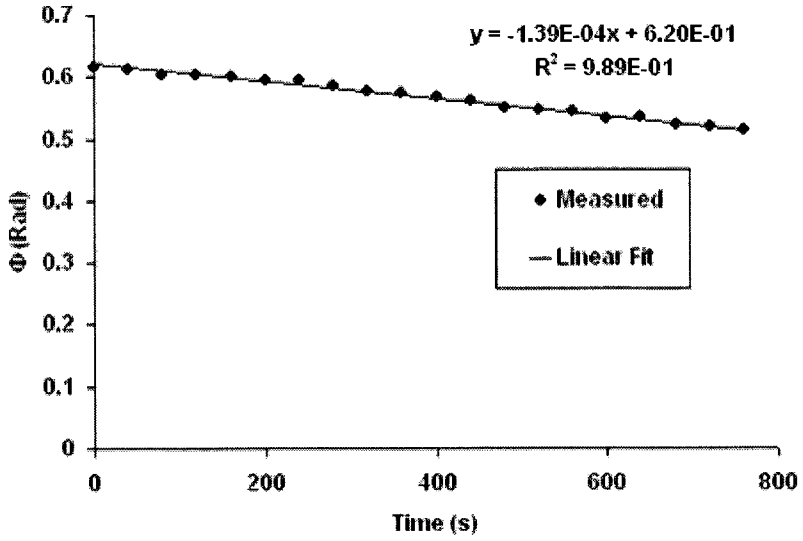

Figure 3.16 The measured maximum Faraday rotation angle vs. time in a **10** km optical fiber while being heated with a **60** $watt$ light bulb.

wire (OPGW) networks (Leeson, 2009) and in locations where the earth's magnetic field is parallel to single photon transmission systems (Brodsky, 2005). By decreasing the maximum Faraday rotation angle in these two systems the BER will also be decreased. Also, this result shows that the resolution and stability of the OFCS are reduced when using long optical fibers.

Chapter 4

Polarization Dynamics in Optical Ground Wire Network

4.1 Optical Ground Wire Network

Optical ground wire networks are installed by power companies around the world. The OPGW is a heavily armored cable incorporated on high-voltage power systems to provide fault protection from lightning strikes and a high-capacity optical fiber network. The cables can withstand most lightning strikes with no damage occurring to the optical fiber. The optical fiber is bundled, helicoidally wound, communication-grade SMF, and is installed to minimize dispersion. The internal structure of a typical OPGW is shown in figure 4.1.

Dampeners are deployed on the OPGW to decrease Aeolian vibrations. Unlike cable swings, Aeolian vibrations result in the collapsing of air around an object. The frequency of the Aeolian vibrations depends on the size of the object the wind is traveling around and the initial speed of the wind. Natural Aeolian frequencies of a typical OPGW are $10 - 80\ Hz$ for a wind speed range of 3.6 to $25.2\ km/h$ (Krispin, 2007).

Previous PMD analysis has shown that aerial fibers experience much larger PMD changes than buried and submarine fibers because of their highly dynamic environmental

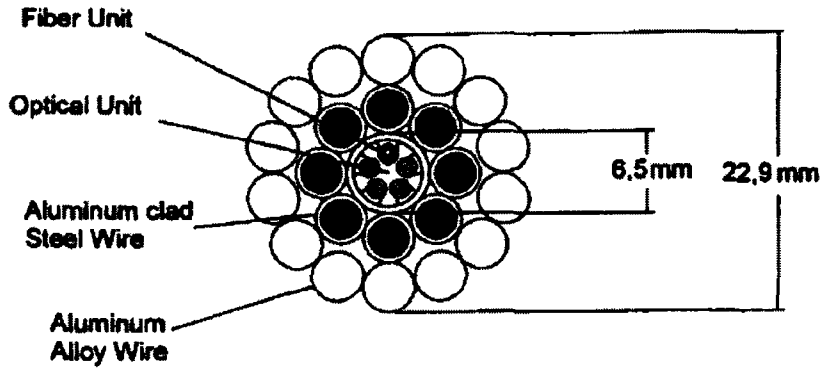

Figure 4.1 The internal structure of a typical OPGW (from Ghannoum, 1995).

exposure (Waddy, 2001, Wuttke, 2003, and Zhang, 2006). However, due to the cost-effective nature of aerial fiber installation and maintenance, it is often the communication system of choice for high-speed and capacity networks.

The motivation to observe the evolution of SOP in the OPGW network comes from previous studies that observed **60** ***Hz*** SOP modulations in OPGW network (Wuttke, 2003, and Kurono, 1999). Wuttke et al. postulate that the origin of the observed **60** ***Hz*** SOP modulations is the result of the **60** ***Hz*** electrical current present near the optical fiber. They indicate that the **60** ***Hz*** polarization modulation may be the result of the Faraday effect. Despite the less than optimal magnetic field configuration of the electrical conductor to cause the Faraday effect, the line sag may generate a parallel magnetic field component to the FUT (Wuttke, 2003).

This study aims to observe the high-speed polarization dynamics in the OPGW network. By this, the nature of the **60** ***Hz*** modulations is observed and a verification of their relation to current for a long period on a commercial OPGW network is concluded. These observations contribute to the polarization studies of aerial fiber by extending observations to the unique case of the OPGW network. The knowledge of the fastest PMD change in an optical fiber link will help to improve PMD monitoring techniques. If the **60** ***Hz*** effect is the result of the Faraday effect, it may also indicate the potential for using OPGW SOP monitoring for a power system structural health monitoring system.

In this chapter, the results of the study of the OPGW are presented. They indicate the electrical currents from the high-voltage power lines lead to high-speed decorrelation of the SOP and non-Gaussian high-speed arc length histogram distributions, which are uncharacteristic of typical aerial fiber. Also, Sun-induced temperature gradients are shown to have a dramatic influence on these high-speed SOP changes during daytime periods with

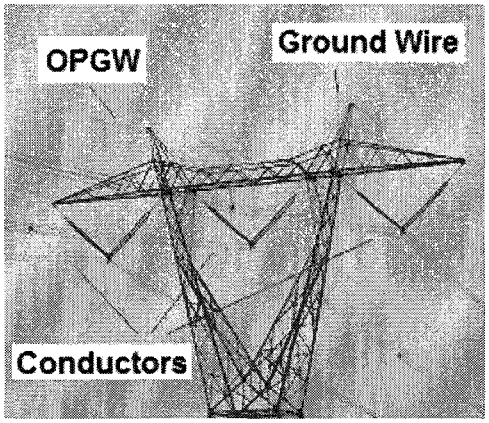

Figure 4.2 The $735\ kV$ high voltage line electricity pylon.

higher solar heating power. The high-speed SOP changes indicate advanced PMD compensation techniques may be required when installing or upgrading to a high-speed OPGW network.

4.2 OPGW Network Field Study

Three field tests were conducted on a commercial OPGW network located in Quebec, Canada. For a summer, a fall, and a brief maintenance period with no electrical current, the SOP changes were monitored. The FUT were $33\ km$ dispersion shifted fibers (DSF) contained in the same OPGW installed on a $735\ kV$ high voltage line system. This particular line was chosen because it often carries very large electrical currents, over $1\ kA$. The$735\ kV$ high-voltage line has three bundles of four subconductors, each bundle carrying one phase of electrical current (Lings, 2005), the electricity pylon is shown in figure 4.2 and its geometric values are listed in figure 4.3.

The laser used was an Agilent 8164A tunable laser at $1550\ nm$ with coherence control activated to decrease reflection-induced power fluctuations. The SOP data was

Nominal Voltage (kV)	No. of Subconductors	Conductor Diameter (cm)	Phase Spacing (m)	Min. Conductor Heights* (m)
735	4	3.5/3.56	15.3/12.8	15.3/14.1

*heights in areas frequented by people including agricultural areas

Figure 4.3 The geometric values of the **735** ***kV*** high voltage line (from Lings, 2005).

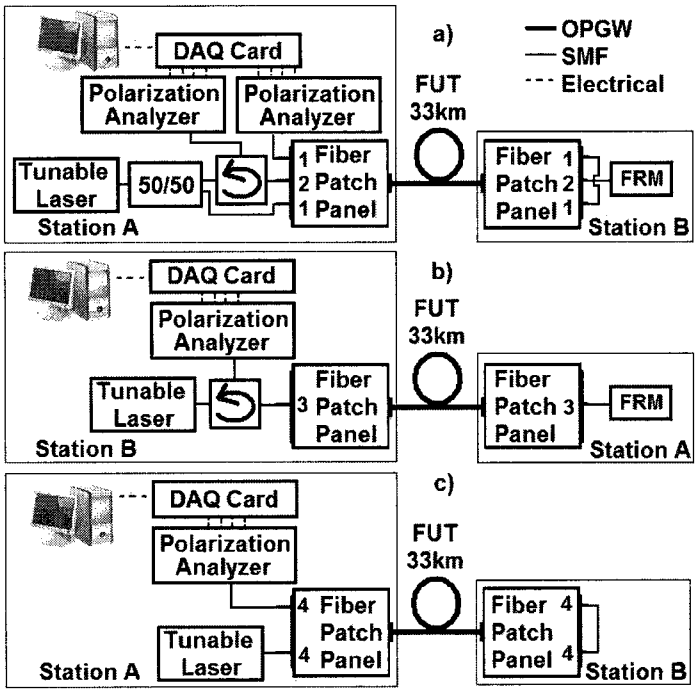

Figure 4.4 The OPGW experimental measurement setups for a) Fiber 1 and Fiber 2 August 1^{st} – 3^{rd}, b) Fiber 3 November 5^{th} – 9^{th}, and c) Fiber 4 July 10^{th}.

acquired at **1** ***kA*** with two Agilent 8509 polarization analyzers and digitized using a National Instruments PCI-6034E DAQ card. The summer period of acquisition occurred August 1^{st}-3^{rd}, the fall acquisition occurred November 5^{th}–9^{th}, and the maintenance period occurred on July 10 from 12:30 to 1:30 pm. The three experimental setups are shown in figure 4.4.

For the summer acquisition period, two separate optical fibers (Fiber 1 and Fiber 2) were tested. The laser signal entered the FUT at Station A. At Station B, Fiber 1 was looped back into the OPGW and Fiber 2 had its signal backreflected with an FRM. Both signals were then acquired at Station A with the polarization analyzers. For the fall period, another optical fiber (Fiber 3) was tested from Station B in the direction of Station A. Similarly to Fiber 2, Fiber 3 was tested using an FRM to backreflect the signal back to Station B. Data was then collected at Station B using a polarization analyzer. For the maintenance period, another optical fiber (Fiber 4) was tested. Similarly to Fiber 1, Fiber 4 was looped back into the OPGW at Station B, and acquired using a polarization analyzer. All SOP data was stored for computational analysis.

4.3 Power Spectrum Analysis

Fast SOP Modulations

To analyze the frequency of the SOP changes, a power spectrum analysis was performed. The power spectrum of the output SOP is one common method of analyzing PMD in a communication system. In chapter 2 it was discussed that dynamic birefringence changes are intimately related to the time varying PMD in a system at a given wavelength. The power spectrums of Fiber 1 and Fiber 2 during the summer period are shown in figure 4.4.

A large $60\ Hz$ spectral component is present in both optical fibers. The frequency of the current in the electrical conductors that run along the FUT is also $60\ Hz$. As previously reported by Wuttke et al., the magnetic field generated by the electrical current carried in the conductors can modulate the SOP by way of the Faraday effect (Wuttke, 2003). The Faraday

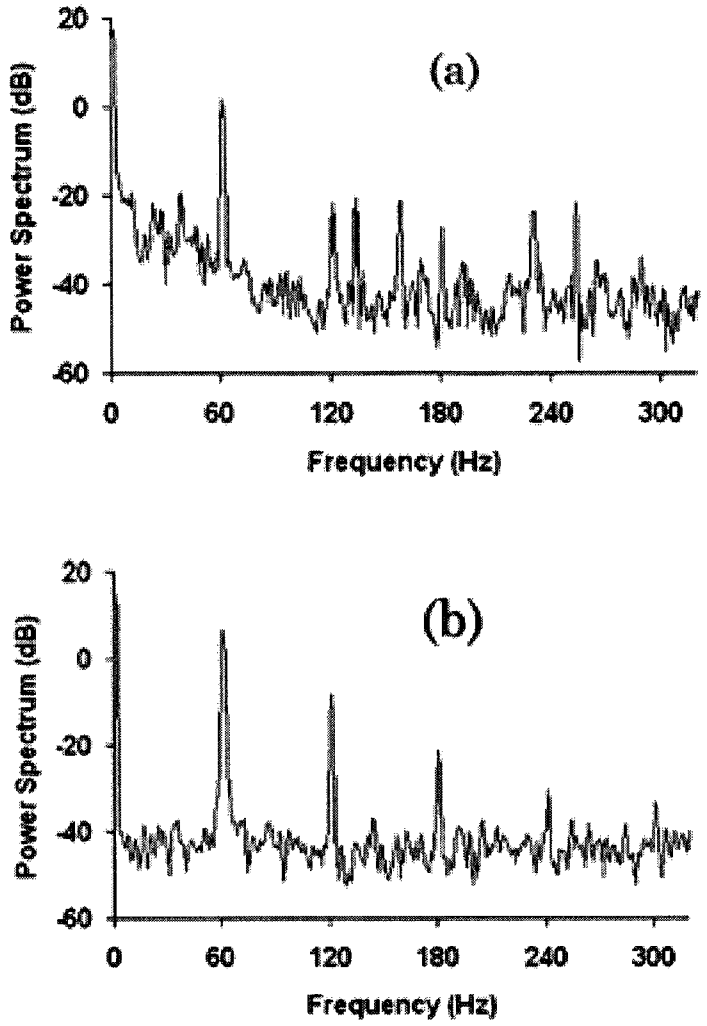

Figure 4.5 The calculated power spectrum of (a) Fiber 1 with no FRM installed and (b) Fiber 2 with FRM installed.

effect can occur at rather low field strengths in long optical fiber. Recall, for a wavelength of $1550\ nm$ dispersion-shifted fiber has a Verdet constant value of $0.53\ rad/m \cdot T$.

More surprising than the existence of the $60\ Hz$ SOP modulation are the $120\ Hz$, $180\ Hz$, $240\ Hz$, and $300\ Hz$ SOP modulations often present in figure 4.4 (b). These are regularly proportional to the $60\ Hz$ modulation. This shows that no higher order magneto-

optic or electro-optic SOP modulating effects, i.e., electro-optic Kerr effect, Voigt effect, etc., are present in the FUT. The proportionality demonstrates that these peaks are harmonics of the $60\ Hz$ SOP modulations. The harmonics are generated by harmonic electrical currents resulting from the power transmission process. The nonlinear voltage/electrical current properties of electrical devices generate the harmonic electrical currents that then result in harmonic magnetic fields (Hydro-Québec, 1999). The harmonic content of the voltage on high-voltage power lines should be below $0.1\ \%$. This ratio was not measured on this high-voltage power line, but it is expected to be slightly higher for the electrical current. The higher-order spectral components are important because they are very high-speed SOP changes. The higher-speed SOP modulations may generate significant PMD modulations, causing error in communication systems because PMD compensation systems are not fast enough to dynamically compensate for the changes.

Time-varying linear birefringence effects can decorrelate the $60\ Hz$ SOP modulations from the electrical current. During the field test, time-varying linear birefringence results from the combination of ambient temperature fluctuations, wind, and solar heating. The FRM minimizes these and other reciprocal birefringence effects. A previous study has also used an FRM to observe the Faraday effect in telecom fiber (Brodsky, 2006). For this reason the FRM was used in the field study.

In figure 4.5 (a), a large spectral base exists until $\sim 100\ Hz$. In figure 4.5 (b), the FRM removes these SOP modulations indicating they are reciprocal in nature, i.e., not magneto-optic. The wind speed was $17\ km/h$ during this period. The natural Aeolian frequency of an OPGW is $10 - 80\ Hz$ for a wind speed range of 3.6 to $25.2\ km/h$ (Krispen, 2007). Because very similar frequencies to the natural Aeolian frequencies are observed and they are reciprocal in nature, the SOP modulations must be the result of Aeolian vibrations.

Figure 4.6 shows the power spectrum of Fiber 1 during the summertime period, Fiber 4 during the maintenance period, and a background measurement taken using $2\ m$ of optical fiber inside Station A. The electrical current Fiber 1 is exposed to is $\sim 860\ A$. The $60\ Hz$ spectral component of Fiber 1 is $100\ (20\ dB)$ times larger than Fiber 4, which has no electrical current. The back-to-back measurement in Station A reveals no $60\ Hz$ background in the measurements. The presence of electrical current is shown to have a significant affect on SOP modulation.

When the electrical current is off, the $60\ Hz$ spectral component is the result of the neighboring high-voltage power lines and/or electrical components. Many high-voltage power lines enter closely at substations and each substation also contains many electrical devices. The power lines and components all generate their own magnetic fields. The

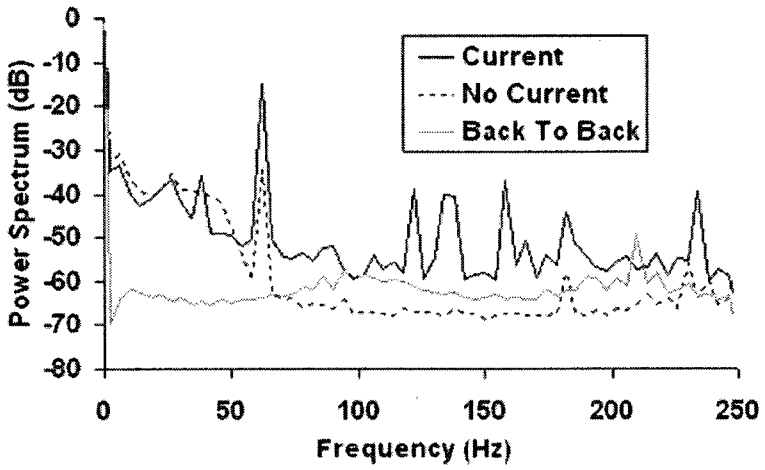

Figure 4.6 The calculated power spectrum for $1\ min$ acquisitions in Fiber 1 measured with an electrical current of $\sim 860\ A$ on August 2, 2007 (solid black line), Fiber 4 measured without electrical current on July 10, 2007 (dashed black line), and a measurement using $2\ m$ of optical fiber inside station A (solid gray line).

combined magnetic fields are also contributing to SOP changes in OPGW networks.

Slow SOP Modulations

A low frequency spectral analysis, $< 1\ Hz$, shows large SOP modulations during all daytimes without heavy cloud cover for all FUT. These fluctuations are most likely due to solar radiation. A previous temperature study of the OPGW showed the inner temperature rises 4^o higher than ambient temperature during daytime periods due to solar radiation (Serizawa, 1999). This temperature-gradient-induced stress in the cable could result in the observed variations in the SOP during the day. The wind does not generate these oscillations because during the nighttime, large wind speeds do not influence the SOP changes in this manner. The $< 1\ Hz$ frequencies observed at night are consistent with the frequency

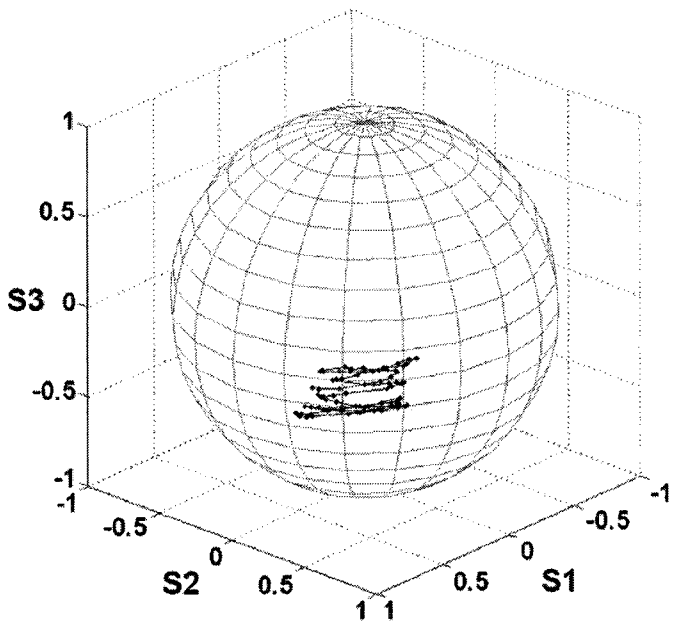

Figure 4.7 The Poincare sphere plotted with 100 normalized points from Fiber 1 during a daytime period. The slow drifting 60 Hz SOP modulations are visible.

previously reported for the wind-induced line oscillations (Wuttke, 2003). The nighttime periods are therefore dominated by slow SOP drift resulting from wind-induced cable swings. A daytime example of the electrical current induced $60\,Hz$ SOP modulations undergoing slow SOP drift in Fiber 1 is plotted on the Poincare sphere in figure 4.7.

4.4 Statistical Analysis of SOP

Ideally, in an optical fiber communication system the SOP would be invariant with time. In long optical fiber, the SOP variations are statistical in nature. Similar to PMD, the statistical distribution of SOP changes can be plotted for different time intervals. This gives the statistical nature of the SOP decorrelation. To calculate this, the arc length traced out on the Poincare sphere in a given time interval, Δt, is used. The arc length is calculated using the following definition:

$$\phi(t, \Delta t) = \cos^{-1}\left[\vec{S}(t) \cdot \vec{S}(t + \Delta t)\right], \qquad (4.1)$$

where $\vec{S}$ is the normalized Stokes vector. The arc length is a measure of interest to PMD compensation design engineers because it quantifies the intensity of the SOP changes over a given time interval. Δt is specifically chosen to reveal the most interesting features of the SOP changes. By using $\Delta t = 2\,ms$ the impact of the electrical current on a very small time scale is observed, by using $\Delta t = 8\,ms$ the largest arc length value caused by the electrical current is observed, and by using $\Delta t = 17\,ms$ the electrical current SOP modulations are minimized to better observe the role of the Aeolian vibrations.

To analyze the statistical distribution $1\,h$ histograms for $\Delta t = 2\,ms, \Delta t = 8\,ms$, and $\Delta t = 17\,ms$ for different electrical current and environmental conditions are calculated. The histograms are shown in figure 4.8.

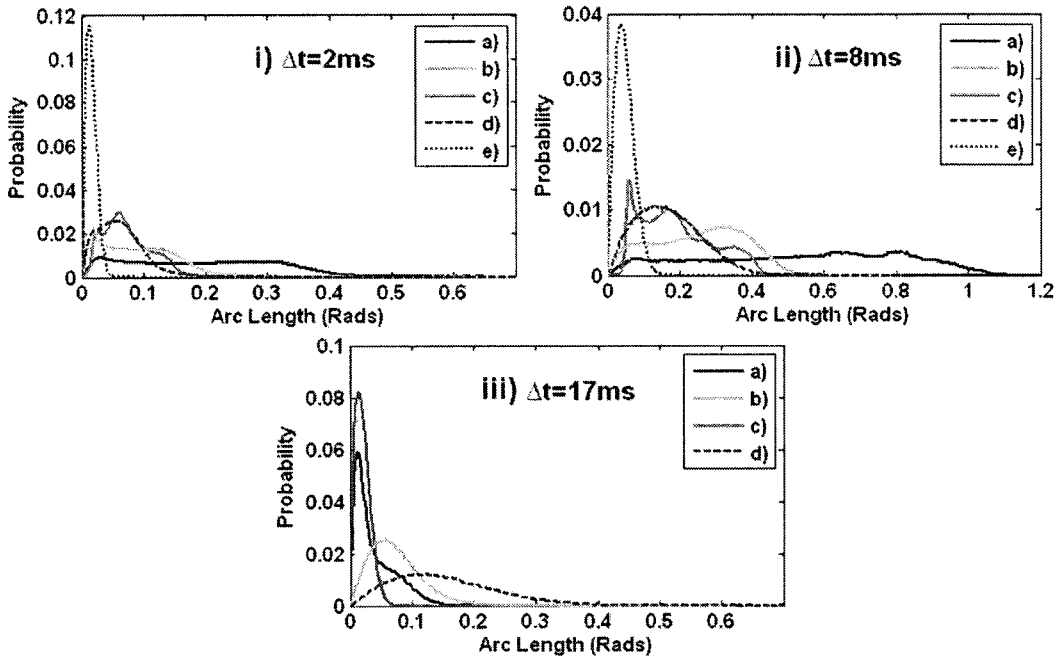

Figure 4.8 The calculated histograms of arc length for different values of Δt during the following environmental and electrical current conditions: a) Fiber 2 ($I = 801\ A$, daytime, $v_{wind} = 28\ km/h$), b) Fiber 1 ($I = 801\ A$, daytime, $v_{wind} = 28\ km/h$), c) Fiber 2 ($I = 612\ A$, nighttime, $v_{wind} = 4\ km/h$), d) Fiber 1 ($I = 612\ A$, nighttime, $v_{wind} = 4\ km/h$), and e) Fiber 4 ($I = 0\ A$, daytime, $v_{wind} = 11\ km/h$), where v_{wind} is the average wind speed.

Figure 4.8 i) shows that in the presence of electrical current the fast polarization changes are much more extreme than when no electrical current is present. This figure shows that to observe all the dynamic SOP features in an OPGW, one must sample on the order of a few milliseconds or less. Figure 4.8 ii) shows that when the $60\ Hz$ modulations are maximized, very large arc lengths for all optical fibers with electrical current exposure are shown. The maximum value in Fiber 1 over these periods is $0.6294\ rad$, and the maximum in Fiber 2 over these periods is $1.1137\ rad$. Figure 4.8 iii) shows that in Fiber 2, the FRM is

minimizing the fast reciprocal SOP modulating effects. The Fiber 1 curves show that other fast reciprocal SOP modulations are present on this time scale. On all time scales, the arc length histogram is a non-Gaussian distribution when electrical current is present. A non-Gaussian distribution is uncharacteristic of typical aerial fiber.

The SOP autocorrelation function (ACF) is a measure of how similar the SOP is over a given time interval. The SOP ACF is calculated using:

$$ACF(\Delta t) = \frac{1}{N}\sum_{k=0}^{N-1} \vec{S}(t_k) \cdot \vec{S}(t_k + \Delta t), \quad (4.2)$$

where N is the total number of points in the measurement time interval. For convenience, our definition assumes that the signal decorrelates within the measurement time, this is known as the bias ACF. The unbiased ACF requires the SOP fill the whole surface of the Poincare sphere within the measurement period. This is not guaranteed to happen in our measurement time interval, so the bias ACF is used.

If current is influencing the SOP, it should decorrelate when current increases. To directly compare current to the SOP decorrelation as a function of time, a method from (Bao, 2004) can be used. For this method, equation 4.2 is used to define t_{half} as $ACF(t_{half}) = 1/2$, where t_{half} describes the time at which the SOP decorrelates 50 %. The change in the way the SOP decorrelates is then described using the inverse $ACF50\%$ defined as follows:

$$ACF50\%(t_{half}) = \frac{T - t_{half}}{T}, \quad (4.3)$$

where at the maximum value of $ACF50\% = 1$, there is the fastest SOP decorrelation possible, and at a minimum value of $ACF50\% = 0$, there is no SOP decorrelation over the time interval, T. $10\ min$ ($T = 600\ s$) time intervals are used for the calculation. The current is at a frequency of $60\ Hz$ and the sampling rate is $1\ kHz$, so $\Delta t = 8\ ms$ is the best choice to observe the influence of the electrical current.

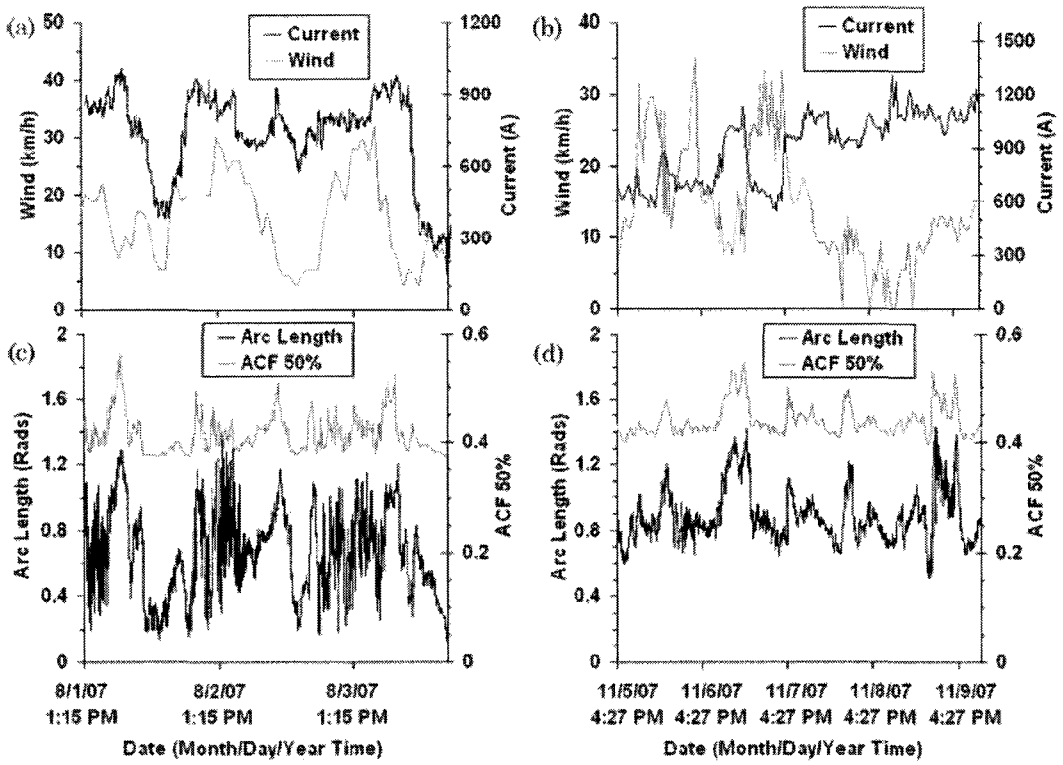

Figure 4.9 The wind and electrical current data plotted for (a) Fiber 2 and (b) Fiber 3. The calculated maximum arc length is plotted with $ACF50\%$ of (c) Fiber 2 and (d) Fiber 3.

Figure 4.9 compares the arc length and $ACF50\%$ to data for the fast-changing environmental factors, i.e., the wind speed and the electrical current carried by the neighboring conductors, for Fiber 2 and Fiber 3.

Figures 4.9 (a) and 4.9 (c) expose a correlation between the arc length and the electrical current during the nighttime periods that is not observed without the FRM installed. The minimizing of temperature fluctuation and wind-induced linear birefringence allows us to observe the magnetic fields' contribution to the polarization changes. As the FRM is not ideal, linear birefringence effects are still observed during the daytime period. The linear birefringence effects are indicated by the fast variations in the arc length. These

variations must be caused by Sun-radiation-induced temperature gradients between the cable core and cable surface because the variations show no apparent correlation to any other environmental factors. The $ACF50\%$ shows that SOP drift is correlated with electrical current during most of the acquisition time. The ACF is shown to decorrelate as electrical current increases despite the presence of the solar gradient effect during the day. This correlation is surprising because the arc length variations are very large here.

It is now worthwhile to look at Fiber 3 to see how decreased solar heating during the late fall affects SOP drift. Figures 4.9 (b) and 4.9 (d) reveal that the nighttime electrical current is correlated with the arc length as observed during the summer period. This is not surprising because Fiber 2 and Fiber 3 both had a FRM installed. There is, however, a major difference in the daytime data between the summer and fall periods. During the day, Fiber 3 does not experience the arc length fluctuations reported in Fiber 2. This is most likely due to the higher solar heating power reaching the OPGW in the summer than in the late fall. Higher solar heating power will induce stronger temperature gradients across the FUT. The $ACF50\%$ shows that SOP drift is correlated with electrical current and wind. This is because the wind reaches higher speeds during the fall period.

Chapter 5

Distributed Polarization Sensing

5.1 Distributed Sensors

The scattering processes in optical fiber are the result of density fluctuations. They arise because fiber glasses are amorphous and often contain dopants. Refractive index is a function of density which leads to microscopic changes in n. If the density fluctuations occur over very small lengths compared to the wavelength of light, one will observe Rayleigh scattering. For this reason Rayleigh scattering is highly wavelength-dependent. The density fluctuations, resulting in the optical fiber scattering processes, are described using the following expression (Boyd, 2003):

$$\Delta\rho = \left(\frac{\partial\rho}{\partial \mathrm{p}}\right)_s \Delta \mathrm{p} + \left(\frac{\partial\rho}{\partial s}\right)_{\mathrm{p}} \Delta s, \tag{5.1}$$

where p is pressure and s is entropy. The first term leads to adiabatic density fluctuations, i.e., acoustic waves, and intern Brillouin scattering. The second term leads to isobaric density fluctuations, i.e., entropy or temperature changes, and intern Rayleigh scattering.

While communications has struggled to overcome the results of modal birefringence, nonlinear effects, and scattering mechanisms, optical fiber sensing has embraced these effects using the optical fiber's vulnerability to extrinsic stress to their advantage. For example, polarization sensing uses birefringence to measure quantities such as strain, temperature, magnetic field, and vibrations.

The distributed nature of optical fiber allows for the development of distributed optical fiber sensors. The most common distributed optical fiber sensors apply either the working principals of optical frequency domain reflectrometry (OFDR), optical coherence topography (OCT), or optical time domain reflectrometry (OTDR). Typically, these methods rely on monitoring different properties of Rayleigh backscattering light. From this they can

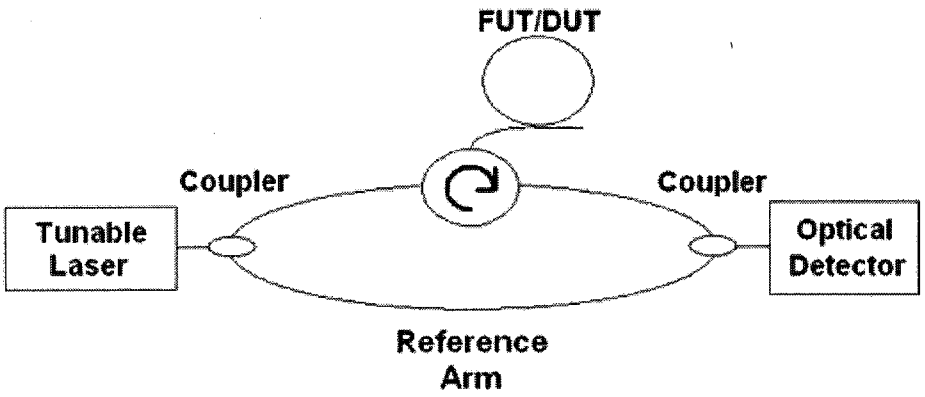

Figure 5.1 The OFDR experimental setup for distributed detection using Rayleigh backscattered light.

determine different information about events along a device under test (DUT) or FUT.

OFDR monitors the change in frequency during a spectral sweep using an interferometer. The time delay resulting from the time of flight of the light signal during the sweep generates a phase shift in the measurement arm. When the phase-shifted backscattered light combines with the light in the reference arm, the two light beams generate a beating frequency which is recorded using a detector. When the fast Fourier transform is performed on the data it reveals the backscattered beam from all positions in the optical fiber. The setup is shown in figure 5.1. OFDR requires a very narrow linewidth because the broader the frequency range the more phase noise. OFDR is also vulnerable to polarization fluctuations and the quality of the frequency sweep of the tunable laser.

OCT can distributively sense using the interference pattern of a low coherence laser. Unlike most conventional interferometer sources which have long coherence lengths (meters), a low-coherence laser will only observe interference patterns within a micrometer range. Here time domain OCT will be discussed; however, frequency detection may also be used with a frequency modulated source. In time domain OCT a mirror is adjusted, possibly

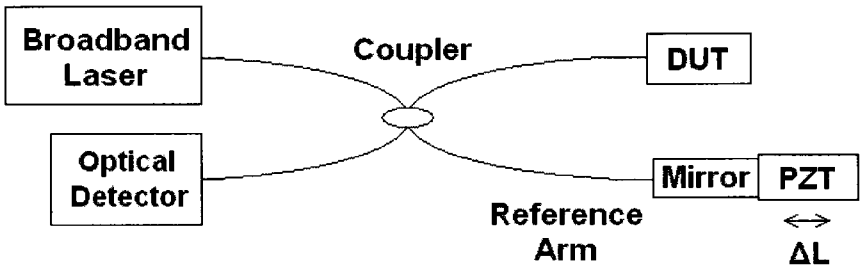

Figure 5.2 The time domain OCT experimental setup for distributed detection using Rayleigh backscattered light.

with a PZT, in the reference arm until the signal from the DUT has a path length difference of less than the coherence length generating interference. Further scanning of the mirror will generate an interference profile of the entire DUT in high resolution. A basic time domain OCT setup is shown in figure 5.2. Time domain OCT is a very slow method, frequency domain acquisition techniques have been used to solve this problem.

OTDR uses timed pulse propagation, which is relatively constant in optical fiber, and Rayleigh backscattered light to distributively monitor an optical fiber length. OTDR requires a higher bandwidth laser and small pulses for improved spatial resolution, but this may limit dynamic range. The experimental OTDR setup is shown in figure 5.3.

For practical applications, each distributed monitoring technique has its appropriate use based on its inherent limitations. OCT is typically used for $< 5\ m$ lengths at micrometer resolutions. OFDR is best suited for ranges of kilometers, to date Rayleigh backscattering has been detected for $< 30\ mm$ over a $5\ km$ range (Koshikiya, 2008). OTDR is best applied to long range (several kilometers) and low-resolution applications. OTDR is therefore most ideal for long optical fiber and communication system applications.

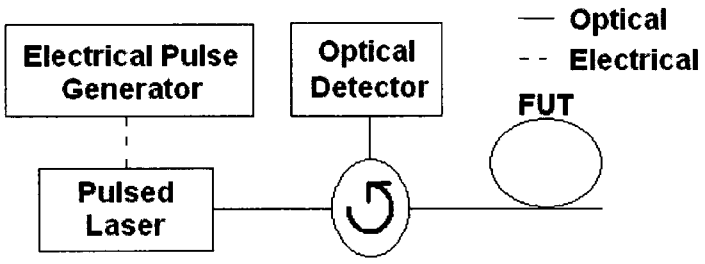

Figure 5.3 The OTDR experimental setup for distributed detection using Rayleigh backscattered light.

5.2 POTDR Magnetic Field Sensing in Long Optical Fiber

When polarimetry is used to obtain polarization information from an OTDR system, a POTDR system is created. As discussed in the introduction, four polarizers are the minimum requirement for measuring the full SOP of a lightwave. If there is a high speed requirement and cost is a factor, however, data can be recorded using a single polarizer. The single polarizer and detector only measure a single intensity. Measuring less than all four Stokes parameters is called incomplete polarimetry. This allows for high-speed acquisition and the recovery of useful information about distributed polarization modulating events. The high-speed acquisition can be used to conduct power spectrum analysis POTDR. This method has been effectively applied to detect vibrations in the $5\ kHz$ region in a $1\ km$ length of SMF (Zhang, 2008b). Power spectrum analysis POTDR is very useful for distributed dynamic analysis because at each position recorded along the optical fiber, a power spectrum is generated. This allows for identification of detected events using their amplitude, location, and frequency information.

POTDR was originally used for magnetic field sensing by (Ross, 1981). In this paper POTDR is used to accurately measure the distributed Faraday rotation at $632.8\ nm$ caused

by a magnetic field of a solenoid in a $14\ m$ length of SMF with no frequency information. Another POTDR study by (Kim, 1982) was used to measure the approximate Verdet constant at $904\ nm$ in a $210\ m$ length of highly twisted SMF and no location information was obtained. Here, power spectrum analysis POTDR will be applied to measure distributed magnetic field. To the best of the author's knowledge, this is the first instance that distributed, frequency resolved magnetic field measurements have been made in long optical fiber.

An important feature of power spectrum analysis POTDR is its ability to accurately diagnose multiple, dynamic birefringent events of the same frequency, after some signal processing. The working principle is that when the light passes an event the magnitude of the respective spectral component will increase a finite amount. Provided no further events occur the component will stay at this new level for the remainder of the FUT. It does not decrease because the light traveling to the end of the optical fiber must return past the event before reaching the detector. When another event of the same frequency occurs it will be detected by further accumulation of the spectral component (Zhang, 2008b) and the events can then be distinguished. Multiple event detection is especially useful when measuring a distributed magnetic field because it generates a series of multiple birefringent events across the optical fiber (Kim, 1982). In the case of a constant magnetic field the result should be an accumulation of the SOP changes over a distance.

The experimental setup for power spectrum analysis POTDR is shown in figure 5.4 as described in (Zhang, 2008). This setup uses a pulsed laser driven by an electric pulse from a function generator. The laser linewidth at the FWHM is $0.08\ nm$. This value is carefully chosen to be broad enough to minimize coherent backscatter noise and narrow enough to prevent depolarization of the pulse due to PMD (Hunttner, 1999). An optical amplifier can

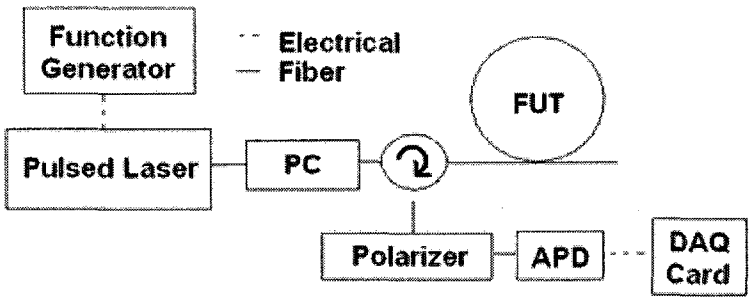

Figure 5.4 The experimental setup for power spectrum analysis POTDR.

also be added to the setup to meet the power requirement for a long or high-loss FUT. A polarization controller is used to vary the input SOP. It is required to maximize the sensitivity to events and minimize the dead spots observed due to the use of only a single polarizer. These dead spots are the result of the beat length of the FUT. The backscattered light was collected via a circulator, passed through a linear polarizer, and the intensity variation was measured by an APD. A high-speed DAQ card with on-board memory is used to obtain the high sampling rate required for spectral analysis POTDR. All connectors must be angled physical contact fiber connectors or physical contact with refractive index matching gel to minimize the detrimental back reflections that can saturate the APD.

For most applications, a distributed magnetic field sensor should be able to function effectively in long optical fiber lengths. Also, due to the Verdet constant, there is an inherent length requirement for low field magnetic sensing. In long optical fiber, however, the method of spectral analysis POTDR using one polarizer suffers from many major issues, i.e., noise, intensity loss, depolarization, etc.. For this reason, additional algorithms and sensing techniques must be included to accurately detect a magnetic field event. A measurement using a $10\ km$ SMF-28 section with a constant $60\ Hz$ magnetic field and a $25\ km$ section of non-zero dispersion shifted fiber (NZ-DSF) with no magnetic field is shown in figure 5.5.

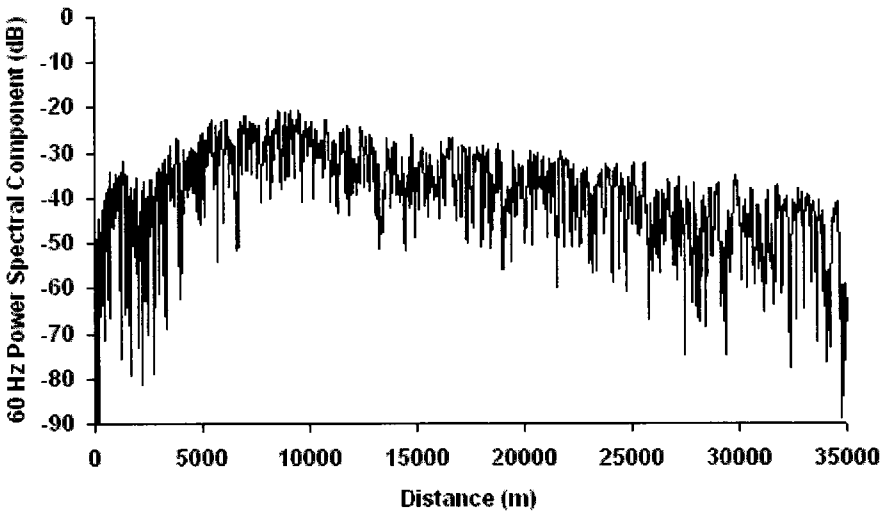

Figure 5.5 The measured $60\ Hz$ power spectral component vs. distance ($5\ m$ resolution) for a $10\ km$ SMF-28 section with constant $60\ Hz$ magnetic field and a $25\ km$ section of NZ-DSF.

For this acquisition, the pulse width was $600\ ns$, the repetition rate was $2.5\ kHz$, a $5\ m$ recorded resolution was used, and 3000 POTDR traces were averaged 10 times. As expected, for the $10\ km$ SMF-28 section with constant $60\ Hz$ magnetic field, an accumulation of the $60\ Hz$ component is observed. However, for the $25\ km$ section of NZ-DSF the $60\ Hz$ component decreases with distance instead of remaining at a constant value. The competition of noise, depolarization, intensity loss, and magnetic field modulation make it hard to diagnose the location of magnetic field events.

Typically, to reduce noise in POTDR sensing the POTDR traces are averaged. In spectral analysis POTDR, however, an averaging of the POTDR traces will decrease the sampling frequency at each position. Thus, trace averaging should only be used when necessary. Here another method that decreases the noise fluctuations and does not affect the sampling frequency at each position will be discussed.

After processing, a power spectrum is acquired at every sampled point. If the points recorded to the DAQ card are at a higher memory resolution than defined by the pulse width, the distributed information is overdetermined. For example, a $600\ ns$ pulse has a spatial resolution of $60\ m$, while the maximum recorded spatial resolution of the DAQ card is $5\ m$. This is a factor 12 larger than the pulse width resolution. The distributed power spectral components can be separated into sets of 12 and individually averaged. Then, the new location of the averaged power spectrum is the center point of the average. A system resolution of $60\ m$ is still maintained.

Essentially, the new averaging technique is a series of spatial averages of the power spectrum. The measurement from figure 5.5 is replotted with spatial averages of period 12 in figure 5.6. The result shows that the averaging does not hinder the accuracy or resolution of

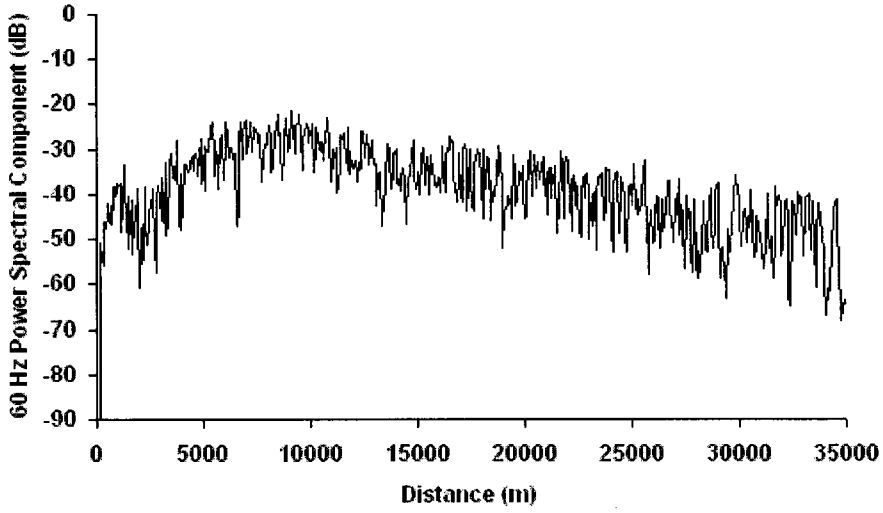

Figure 5.6 The $60\ Hz$ power spectral component POTDR, with a spatial averaging of period 12 ($60\ m$ resolution), measuring a distributed magnetic field in a $10\ km$ SMF-28 section with constant $60\ Hz$ magnetic field and a $25\ km$ section of NZ-DSF.

the acquisition system but can decrease the recorded noise. The reduction of noise is very beneficial for improving event detection. The limitation of this method is the sampling rate and size of the on-board memory of the DAQ card. These parameters define the period at which the spatial averaging can be performed. Next, a new method that can eliminate the influences of depolarization and intensity loss from long optical fiber pulse propagation will now be discussed.

During a POTDR test, the information about a birefringent event that occurs at the beginning of a long FUT will be contained in the power spectrum of an entire FUT. The magnitude of this event will be a constant amplitude at the beginning of the optical fiber and will stay near a constant value, provided no depolarization or significant intensity loss. Therefore, if an event is intentionally induced at the beginning of the optical fiber using a polarization modulating device (example: PZT polarization controller), it will contain information about the distributed affect of depolarization and intensity loss. This information can then be used to correct the distributed amplitude of the signal frequency.

In this experiment, an optical fiber-delay line should be added before the induced event to ensure that it is not within the small dead zone that exists at the beginning of the FUT. The PZT drive frequency is chosen carefully so that the drive frequency and harmonics are dissimilar from the detected signal frequency, and not convoluted by another event of the same frequency already existing in the FUT. A constant AC drive voltage is used so any variation in the drive frequency bin is due to the influences of depolarization and intensity loss. After processing, the amplitude of the distributed spectral component at the measured signal frequency can be rescaled by the amplitude of the distributed spectral component of the PZT frequency. The proper location and relative magnitude of the SOP modulation can then be determined. The setup is shown in figure 5.7.

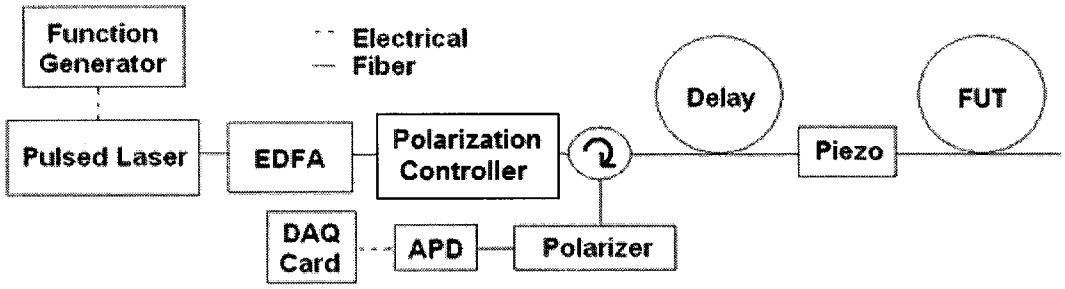

Figure 5.7 The experimental setup for induced event power spectrum analysis POTDR.

An example of the induced event spectrum is shown in figure 5.8 a). The plot shows that the intensity is changing over the length of optical fiber. It is important to note that the slope will not always be linear. Optical components, splices, and bend induced loss and depolarization could all influence the slope. In figure 5.8 b) an example of the rescaled $60\ Hz$ power spectral component vs. distance is shown. The original plot is shown in figure 5.5. The rescaled $60\ Hz$ spectrum vs. distance is for a $10\ km$ SMF-28 section with constant $60\ Hz$ magnetic field and a $25\ km$ section of NZ-DSF. As shown, the constant magnetic field increases the magnitude of the $60\ Hz$ component for the first $10\ km$ of optical fiber. From theory in unperturbed optical fiber Faraday rotation is linearly proportional to distance so this slope should be logarithmic. At $10\ km$ there is a plateau for the rest of the FUT indicating no additional $60\ Hz$ SOP modulation in the rest of the FUT. This result shows an induced event spectrum analysis POTDR can accurately detect magnetic field events in long optical fiber.

Sensitivity

Now that a magnetic field event has been effectively diagnosed in long optical fiber lengths, the maximum sensitivity can be measured for different optical fiber types.

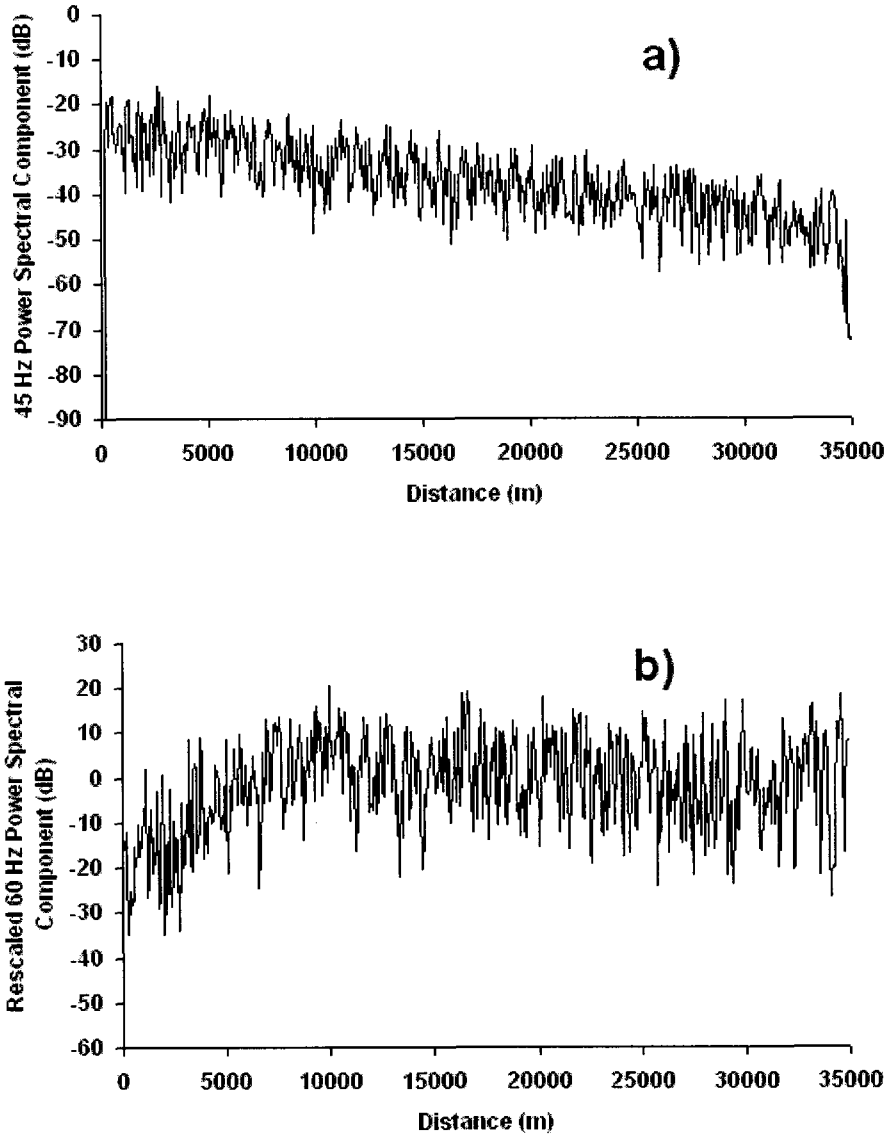

Figure 5.8 a) The $45\ Hz$ power spectral component vs. distance for a PZT induced event at the beginning of the FUT and b) the rescaled $60\ Hz$ power spectral component vs. distance for a $10\ km$ SMF-28 section with constant $60\ Hz$ magnetic field and a $25\ km$ section of NZ-DSF.

Specifically, 10 km lengths of SMF-28 and NZ-DSF will be compared. For these measurements, the input SOP is carefully optimized so the maximum sensitivity is obtained. For both measurements, the experimental settings used are: a pulse width of $600\ ns$, $2.5\ kHz$ repetition rate, $5\ m$ recorded resolution, 3000 POTDR traces were averaged 10 times, and a spatial averaging of period 12. The measurement results are shown in figure 5.9. Assuming that the applied magnetic field and linear birefringence is constant across the entire FUT, the system response should be linear with distance. The first assumption is valid due to the negligible thickness of the optical fiber on the spool. The second assumption is valid because the system response is calculated over a long optical fiber length. For these reasons, linear least squares fits of the data sets are used. The calculated slopes are: $6.62 \times 10^{-4}\ V_{rms}/(V_{rms} \cdot m)$ for the SMF-28 and $8.23 \times 10^{-4}\ V_{rms}/(V_{rms} \cdot m)$ for the NZ-DSF. To calculate the sensitivity of the POTDR system for both optical fiber types, it is assumed that the magnetic field and the Verdet constant across the optical fiber length is a constant. This assumption is validated by the approximate linearity of both signals over the tested lengths. Using that the applied magnetic field was $1.06 \times 10^{-4}\ T$ for both the measurements and the two slopes from each respective linear fit a sensitivity of $6.25\ V_{rms}/(V_{rms} \cdot m \cdot T)$ for SMF-28 and a sensitivity of $7.76\ V_{rms}/(V_{rms} \cdot m \cdot T)$ for NZ-DSF are found. The increased sensitivity in NZ-DSF is most likely due to its lower PMD value ($\leq 0.04\ ps/\sqrt{km}$) than SMF-28 ($\leq 0.06\ ps/\sqrt{km}$). The higher PMD value will quench the magnetic field response across long optical fiber lengths.

5.3 POTDR OPGW Network Field Study

A field test was conducted on April 21, 2009. The FUT was DSF contained in the same 33 km OPGW tested in chapter 4. The setup used was a pulsed laser driven by a

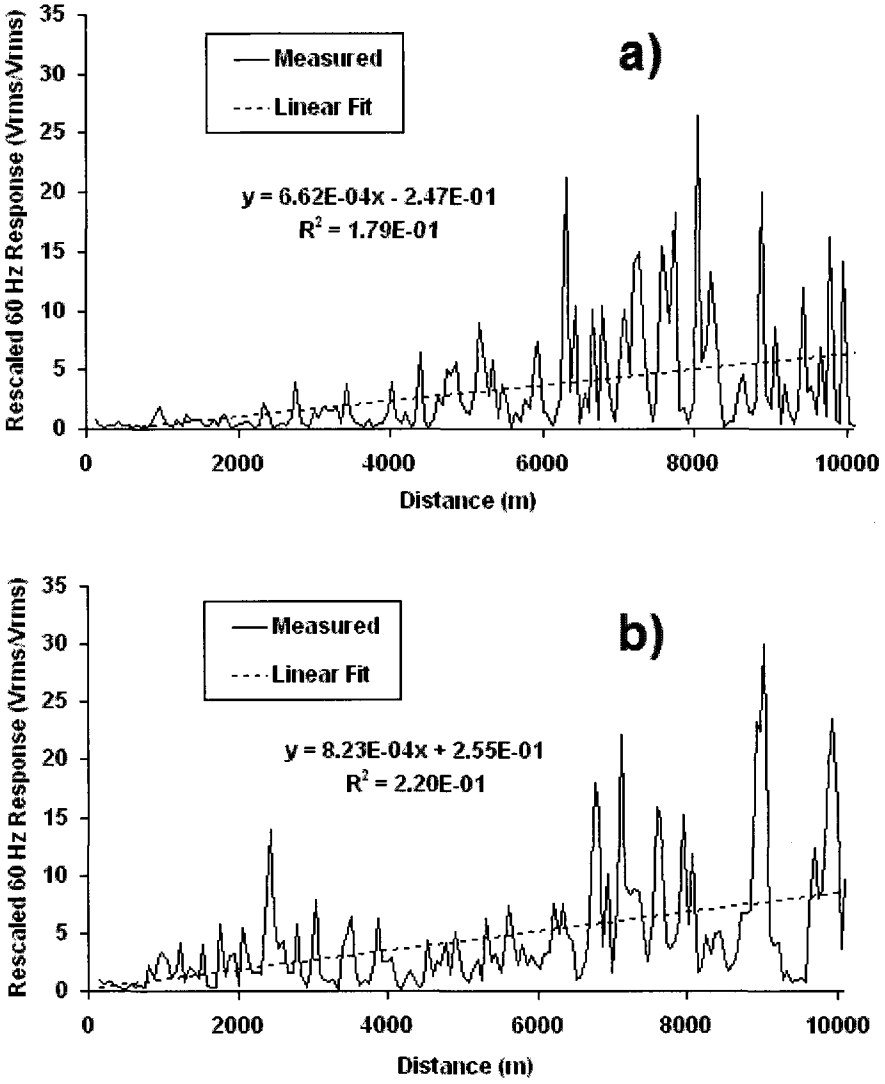

Figure 5.9 The distributed magnetic field sensitivity measurement in a) SMF-28 and b) NZ-DSF for 10 km optical fiber sections.

function generator that generated the electrical pulse. The pulse was amplified by a C-band EDFA. The amplification was required to generate a pulse of high enough optical power to overcome the pre-installed physical connection fiber connector and to reached the end of the FUT. A polarization controller was used to vary the input SOP. Refractive index matching

gel (Thorlabs) had to be used at the fiber patch panel on the physical connection fiber connector in Station 1 to couple enough of the pulse into the FUT and not to saturate the sensitive APD detector. The backscattered light was collected via a circulator, passed through a polarizer, and the intensity variation was measured by an APD. The polarization controller was varied to maximize the sensitivity to magnetic field events. The experimental setup is shown in figure 5.10. The test setting were: a pulse width of $600\ ns$, $2.5\ kHz$ repetition rate, $5\ m$ recorded resolution, 3000 POTDR traces were averaged 10 times, and a spatial averaging of period 12.

The strongest spectral component observed was $60\ Hz$ distributed along the FUT. The $60\ Hz$ power spectral component vs. distance is plotted in figure 5.11. This spectral component increases and decreases across the FUT, indicating the presence of $60\ Hz$ distributed in a number of locations along the FUT. One interesting feature is that only small fluctuations exist for two large regions across the fiber ($8000\ m - 12000\ m$ and $21000\ m - 27000\ m$). This decrease in signal variation also occurs in other spectral bins.

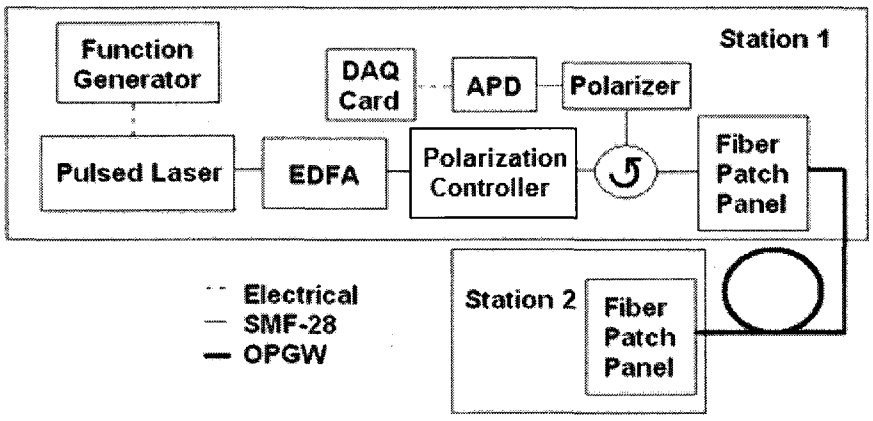

Figure 5.10 The POTDR experimental setup for distributed SOP analysis of the OPGW network.

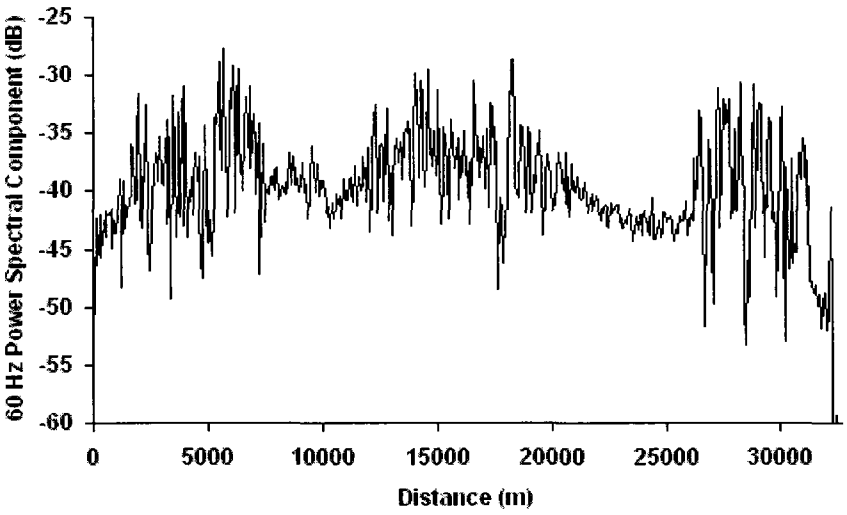

Figure 5.11 The OPGW measured **60** Hz power spectral component vs. distance.

This is possibly caused by the interaction of PMD and the optical Kerr effect due to high pulse peak power, **0.6** W. The optical Kerr effect and intrinsic birefringence can interact to optically modulate the probe beam (backscatter signal) in the presence of interaction between a high pump power (pulse) because it creates mode coupling (Parvaneh, 2000). Therefore, the optical Kerr effect and the magnetic field induced birefringence could be causing the observed modulating effect. Further investigation into the nature of this effect is required.

Due to the depolarization and power loss, the location of the 60 Hz magnetic field events could not be accurately recovered. This result indicates that a different method such as complete polarimetry spectrum analysis POTDR or induced event spectrum analysis POTDR should be used to monitor OPGW systems.

It is important to note, although a **60** Hz signal is distributively detected in the OPGW, from chapter 4, it is known that the POTDR system cannot diagnose magnetic field events from vibrational events, i.e., Aeolian vibrations or Lorentz force vibrations. Linear birefringence caused by a vibration could generate a **60** Hz event that will convolute the

60 Hz magnetic field modulations. Also, due to the linear birefringence dependency of the Faraday effect, a vibrational event can change the magnitude of the magnetic field modulation. This change could be detected as a false magnetic field event. Therefore, to accurately detect distributed events in the OPGW, both power spectrum analysis and FRM detection should be used. This can be easily implemented because there are multiple fibers available in the OPGW bundles. POTDR and FRM detection can be done using two different fiber in the same OPGW. By this method, accurate location, detection, and diagnosis of a magnetic field event can be accomplished. Diagnosis of false positive events is very important for an effective structural health monitor system.

Chapter 6

Conclusion

6.1 Thesis Outcomes

A novel sensitive OFCS based on the Faraday effect is presented. This sensor uses two FRM to form a cavity. The cavity amplifies the inherently low-phase modulation caused by a longitudinal magnetic field while still maintaining high insensitivity to linear birefringence effects. By using Sagnac loop interferometry, a $10\ dB$ FRM cavity, and differential detection, a minimum response of $10.669\ A_{rms} \cdot t/\sqrt{Hz}$ for a frequency of $50\ kHz$ can be obtained with a highly linear response to current. This sensor is well-suited for temperature stable, low-field, high-frequency current sensing. With the proper choice of detectors and DAQ card, a sensor of this type could measure MHz or even GHz currents with similar sensitivities.

It is shown that the maximum Faraday rotation angle in a given fiber with a constant birefringence is input SOP insensitive. This improves stability of polarization rotation measurements of DC magnetic fields where SOP drift is present before the FUT. A quenching of the maximum Faraday rotation angle has been shown to occur in long optical fiber due to linear birefringence. This indicates that high birefringence optical fiber may be required in communication systems to minimize Faraday rotation, i.e., increased BER, where magnetic fields exist.

The SOP changes in an OPGW network have been attributed to the following surrounding environmental conditions: ambient temperature changes, wind, Sun-induced temperature gradients, and electrical current. High-speed arc length histograms show non-Gaussian distributions in the presence of electrical current, which are uncharacteristic of typical aerial fiber. Evidence that the highest-speed polarization changes are attributed to the

high-voltage power line, i.e., the electrical current, using the SOP autocorrelation function is shown. The SOP ACF becomes decorrelated when the electrical current increases, demonstrating PMD compensation at speeds of $3\ ms$ or less may be required when installing or upgrading high-speed OPGW networks above $10\ Gbits/s$.

Power spectrum analysis POTDR has been shown to work in long optical fiber. The noise in power spectrum analysis can be decreased by a spatial average of the distributed power spectrum. This method does not hinder the resolution or accuracy of the measurement when data points recorded with a resolution smaller than the pulse width resolution. A study of an OPGW network using spectral analysis POTDR has revealed distributed $60\ Hz$ polarization modulation. However, spectral analysis POTDR could not accurately detect the location of magnetic field events with a single polarizer. An alternative method such as for induced event power spectrum analysis POTDR may solve this problem. This method can accurately measure the location of magnetic fields with a single polarizer by rescaling the spectral component of the signal frequency with the spectral component of an induced PZT event at the beginning of the FUT. A magnetic field sensitivity of $6.25\ V_{rms}/(V_{rms} \cdot m \cdot T)$ for SMF-28 and $7.76\ V_{rms}/(V_{rms} \cdot m \cdot T)$ for NZ-DSF using this method is found. The discrepancy in the sensitivity is most likely due to the lower PMD values of NZ-DSF.

When distributively monitoring the magnetic field in the OPGW, for structural health monitoring, power spectrum analysis POTDR and FRM detection are both required to accurately distinguish magnetic field events from a vibration event, i.e., Aeolian vibration or Lorentz force. The diagnosis of false positive events can be accomplished by combining the two methods in two fibers contained within the OPGW cable.

6.2 Future Work

The study of the FRM cavity Sagnac loop interferometric OFCS was limited by the maximum frequency output of the power source that generates the current. The principle of $MHz - GHz$ magnetic field detection should be verified with a high speed power source. GHz acquisition will also require a higher-speed DAQ card and optical detectors. The use of a lower central wavelength: broadband source, optical fiber, and components, could greatly increase the sensitivity of this sensor. This is due to the relation between the Verdet constant and frequency, $v \propto v^2$. Optimization of the differential detection scheme would include balancing the arms of the two output channels using variable attenuators and implementing balance detection. Also, other detection schemes could be explored.

Future work investigating the SOP dynamics of the OPGW should be distributed in nature. Therefore, improving the method of spectral analysis POTDR would be highly beneficial. More information then is provided from the induced event method could be

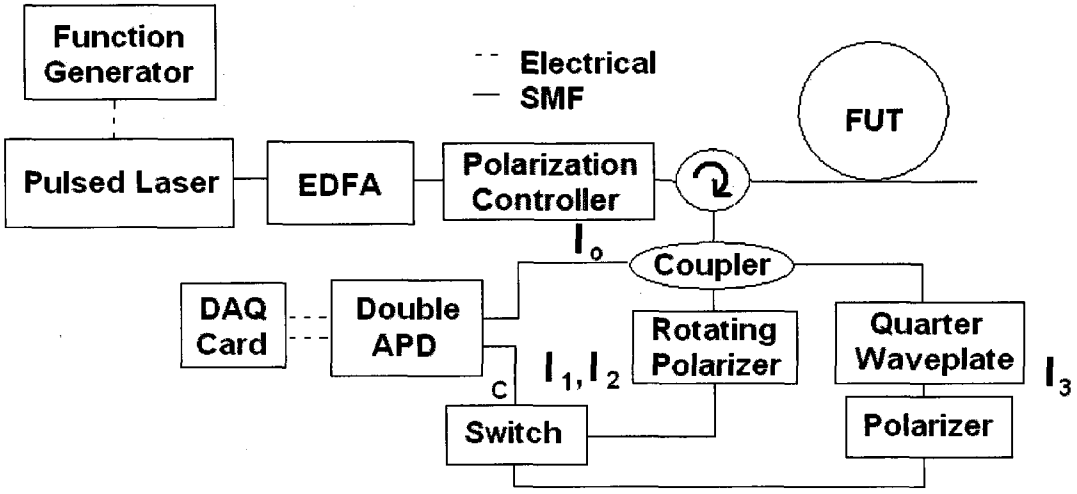

Figure 6.1 The experimental method of acquiring Stokes parameters consecutively for spectral analysis POTDR.

invaluable to a study of the OPGW. The future work in spectral analysis POTDR could benefit from the detection of all four Stokes parameters. The method of complete polarimetry would require high-speed DAQ with at least four channels (see section 1.2 on polarimetry). Complete POTDR would included information of the distributed intensity, DOP, and the full SOP information. Another method that acquires all four Stokes parameters is shown in figure 6.1. In this method, all four Stokes parameters are recorded consecutively. This method is an alternative to complete polarimetry, using only two detectors. It measures the distributed intensity and could approximate the distributed DOP in a quasi-static optical fiber.

Appendix

The AC phase modulation caused by the current is $\phi_C = \Phi \cos \omega_C t$, where for a double pass $\Phi = 4\kappa INL$ and $\kappa = vB/(I \cdot N)$. The four optical paths in the Sagnac loop interferometer with a single reflection is as follows (Bowers, 1982):

$$E_{CW} = \frac{\sqrt{\alpha}}{4} E_o \cos[\omega_o t + \phi_{CW} - \phi_C(t - \tau_S)], \quad \text{(A.1)}$$

$$E_{CCW} = \frac{\sqrt{\alpha}}{4} E_o \cos[\omega_o t + \phi_{CCW} - \phi_C(t - \tau_L)], \quad \text{(A.2)}$$

$$E_S = \frac{\sqrt{\alpha}}{4} E_o \cos[\omega_o t + \phi_S - \phi_C(t - \tau_S)], \quad \text{(A.3)}$$

$$E_L = \frac{\sqrt{\alpha}}{4} E_o \cos[\omega_o t + \phi_L - \phi_C(t - \tau_L)], \quad \text{(A.4)}$$

where α is the loss of the system, which is assumed to be constant for all four paths, E_o is the input electric field, ω_o is the central frequency of the source, ϕ_{CW}, ϕ_{CCW}, ϕ_S, and ϕ_L, are the phases of the CW path, CCW path, short path, and long path at the detectors, respectively, and τ_S and τ_L are the short path and long path time delay from the FUT to the detector, respectively. The four optical paths are shown in figure A.1.

By using the broadband source the parasitic interference terms from the long and short paths are suppressed; therefore, the output intensity of the interferometer is expressed as (Jang, 2002):

$$I = \langle E_S^2 \rangle + \langle E_L^2 \rangle + \langle E_{CW}^2 \rangle + \langle E_{CCW}^2 \rangle + 2\langle E_{CW} \cdot E_{CCW} \rangle, \quad \text{(A.5)}$$

$$I = \frac{\alpha}{8} E_o^2 \left[1 + \frac{1}{2} \cos[\phi_b + \Delta\phi_C]\right], \quad \text{(A.6)}$$

where $\phi_b = \phi_{CW} - \phi_{CCW}$ and $\Delta\phi_C = \phi_C(t - \tau_L) - \phi_C(t - \tau_S)$. Defining $\tau_{tot} = \tau_L + \tau_s$ and $\tau_{rel} = \tau_L - \tau_S$, the differential phase is:

$$\Delta\phi_C = 2\Phi \sin\left\{\omega_C \left(t - \frac{\tau_{tot}}{2}\right)\right\} \cdot \sin\left\{\frac{\omega_C \tau_{rel}}{2}\right\}, \quad \text{(A.7)}$$

Substituting equation A.7 into equation A.6 and considering the two output signals vary by a constant phase shift π:

$$I = \frac{\alpha}{4} I_o \left[1 \pm \frac{1}{2} \cos\left[\phi_b + 2\Phi \sin\left\{\omega_C \left(t - \frac{\tau_{tot}}{2}\right)\right\} \cdot \sin\left\{\frac{\omega_C L_d n}{2c}\right\}\right]\right], \quad \text{(A.8)}$$

where I_o is the intensity of the light source at the input fiber, $\tau_{rel} = L_d n/c$, L_d is the length of the fiber-delay line, n is the refractive index of the fiber core, and c is the speed of light in free space.

Now assuming that the phase bias is set to quadrature, $\phi_b = \pi/2$, the length of the delay line is optimized for the frequency of magnetic field, $\omega_C = \pi c/Ln$, and the applied magnetomotive force is low such that $\Phi \ll 1$ then:

$$I \cong \frac{\alpha}{4} I_o \left[1 \mp 2\Phi \sin\left\{\omega_C \left(t - \frac{\tau_{tot}}{2}\right)\right\}\right], \quad \text{(A.9)}$$

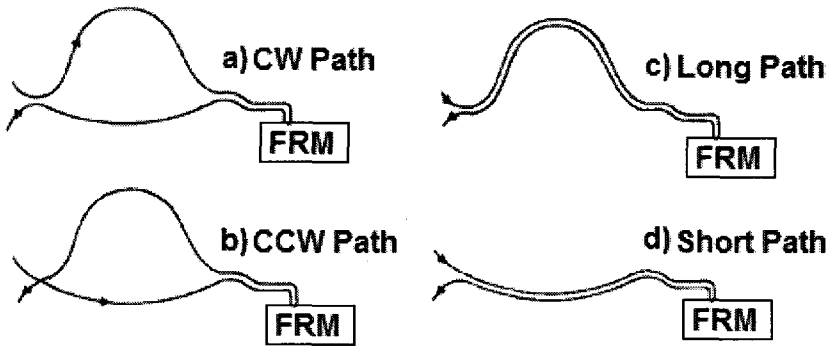

Figure A.1 The four optical paths in the Sagnac loop interferometer with a single reflection. (modified from Bowers, 1982)

References

Agilent Technologies, *HP 8509B Lightwave Polarization Analyzer Product Overview* (1993).

Agilent Technologies, *Agilent 8509A/B Lightwave Polarization Analyzer User's Guide* (2001).

G. P. Agrawal, *Fiber-Optic Communication Systems 3rd edition*, 2002 Wiley, New York.

G. P. Agrawal, *Nonlinear Fiber Optics 3rd edition*, 2001 Academic Press, San Diego.

X. Bao, D. Waddy, L. Chen, "Polarization fluctuations in field fibers," IEEE LEOS **1**, 82–83 (2004).

J. Blake, P. Tantaswadi, R. T. de Carvalho, "In-Line Sagnac interferometer current sensor", IEEE Trans. Power Deliv. **11**, 116-121 (1996).

J. E. Bowers, "Fiber-optical sensor for surface acoustic waves," Appl. Phys. Lett. **41**, 231-233 (1982).

R.W. Boyd, *Nonlinear Optics*, 1992 Academic Press, London.

M. Brodsky, M. Boroditsky, M. D. Feurer, A. Sirenko, "Effect of a weak magnetic field on quantum cryptography links," Proc. ECOC **6**, 19-20 (2005).

M. Brodsky, A. A. Sirenko, A. Zavriyev, A. Trifonov, "Faraday effect in long telecom fibers with randomly varying birefringence," OFCC, 1-3 (2006)

J. Buck, *Fundamentals of Optical Fibers*, 1995 Wiley, New York.

C. Chen. *Foundations for Guided-Wave Optics*, 2006 Wiley, New Jersey.

J. H. Chow, D. E. McClelland, M. B. Gray, "Backscatter-immune, polarization managed, all fiber Sagnac sensing interferometer," Opt. Exp. **15**, 3110-3119 (2007).

J. L. Cruz, M. A. Andres, M. V. Hernandez, "Faraday effect in standard optical fibers: dispersion of the effective Verdet constant," Appl. Opt. **35**, 922-927 (1996).

J. N. Damask, *Polarization Optics in Telecommunications*, 2004 Springer, New York.

N. B. Ekreem, A. G. Olabi, T. Prescott, A. Rafferty, M. s. J. Hashmi, "An overview of magnetostriction, its use and methods to measure these properties," Jour. Mater. Process. Technol. **191**, 96-101 (2007).

E. Ghannoum, J. P. Chouteau, M. Miron, S. Yaacoub, K. Yoshida "Optical Ground Wire for Hydro-Quebec's telecommunication network," IEEE Trans. Power Deliv. **10**, 1724-173 (1995).

D. H. Goldstein, *Polarized Light 2nd Edition*, 2003 Marcell Decker, New York .

K. T. V. Grattan and B. T. Meggitt (Eds.), *Optical Fiber Sensor Technology: Fundamentals*, 2000 Kluwer Academic, Dordrecht.

J. Hecht, *Understanding Fiber Optics 5th Edition*, 2005 Prentice Hall, New Jersey.

B. Hunttner, B. Gisin, and N. Gisin, "Distributed PMD measurement with a polarization-OTDR in optical fibers," J. Lightwave Technol. **17**, 1843-1848 (1999).

Hydro-Québec, *Characteristics and Target Values of the Voltage Supplied by Transmission System* (2001).

T. S. Jang, S. S. Lee, I. B. Kwon, W. J. Lee, J. J. Lee, "Noncontact detection of ultrasonic waves using fiber optic Sagnac interferometer," IEEE Trans. Ultrason., Ferroelect., Freq. **49**, 767-775 (2002).

I. P. Kaminow and T. L. Koch (Eds.), *Optical Fiber Telecommunications IIIA*, 1997 Academic Press, San Jose.

B. Y. Kim, D. Park, S. S. Choi, "Use of polarization-optical time domain reflectometry for observation of the Faraday effect in single-mode fibers," IEEE Jour. Quan. Elec. **18**, 455-456 (1982).

Y. Koshikiya, X. Fan, F. Ito "Long range and cm-level spatial resolution measurement using coherent optical frequency domain reflectometry with SSB-SC modulator and narrow linewidth fiber laser," **26**, 3287-3294 (2008).

H. Krispin, S. Fuchs, P. Hagedorn, "Optimization of the efficiency of Aeolian vibration dampers," PowerAfrica, 1–3 (2007).

M. Kurono, M. Kuribara, K. Isawa, "Field measurements and a study of transient state of polarization produced in OPGW by lightning," **128**, 55-64 (1999).

J. Leeson, X. Bao, A. Coté, "Polarization dynamics in optical ground wire (OPGW) network," Appl. Opt. **48**, 2214-2219 (2009).

J. Lenz and S. Edelstein. "Magnetic sensors and their applications," IEEE Sens. Jour. **6**, 631-649 (2006).

T. H. Lin, W. W. Lin, M. H. Chen, S. C. Huang, "Fiber-optic current sensor using passive demodulation interferometric scheme," Fiber Integr. Opt. **18**, 1096-4681 (1999).

R. Lings, "Overview of transmission lines above 700 kV," Power Engineering Society Inaugural Conference and Exposition in Africa, 33–43 (2005).

C. R. Menyuk and A. Galtarossa (Eds.), *Polarization Mode Dispersion*, 2005 Springer, New York.

J. Miguel and L. Higuera (Eds.), *Handbook of Optical Fibre Sensing Technology*, 2002 Wiley, West Sussex.

F. Parvaneh, V. A. Handerek, A. J. Rogers, "Frequency-derived distributed optical-fiber sensing technique: theory and characterization," Appl. Opt. **39**, 3032-3043 (2000).

D. Phelan, A. Shearer, O. Ryan (Eds.) *High Time Resolution Astrophysics*, 2007 Springer, Netherlands.

J. Prat and J. Comellas, "Dispersion-shifted fiber polarization scrambler based on Faraday effect," IEEE Photo. Tech. Lett., **11**, 845-847 (1999).

J. N. Ross, "Measurement of magnetic field by polarization optical time-domain reflectometry," Elec. Lett. **17**, 596-597 (1981).

H. Sabert and E. Brinkmeyer "Passive birefringence compensation in a frequency comb generator based on a linear fibre optical delay line," Electron. Lett. **30**, 812-814 (1994).

Y. Serizawa, M. Myoujin, S. Miyazaki, K. Kitamura, "Transmission delay variations in OPGW and overhead fiber-optic cable links," IEEE Trans. Power Deliv. **12**, 1415–1421 (1997).

A. M. Smith, "Optical fibres for current measurement applications," Opt. Las. Techn. **12**, 25-29 (1980).

E. Udd, *Fiber Optic Sensors: An Introduction for Engineers and Scientists 2nd Edition*, 1990 Wiley, New York.

D. Waddy, P. Lu, L. Chen, X. Bao, "Fast state of polarization changes in aerial fiber under different climatic conditions," IEEE Photon. Technol. Lett., **13**, 1035–1037 (2001).

T. Wang, C. Luo, S. Zheng, "A fiber optic current sensor based on differentiating Sagnac interferometer," IEEE Trans. Instrum. Meas. **50**, 705-708 (2001).

X. Wang, S. Chen, Z. Du, C. Shi, J. Chen, "Experimental study of some key issues on fiber-optic interferometer sensors detecting weak magnetic field," IEEE Sens. Jour. **8**, 1173-1179 (2008).

P. Williams, A. Rose, G. Day, T. Miller, M. Deeter, "Temperature dependence of the Verdet constant in several diamagnetic glasses," Appl. Opt. **30**, 1176-1178 (1991).

J. Wuttke, P. Krummrich, J. Rosch, "Polarization oscillations in aerial fiber caused by wind and power-line current," IEEE Photon. Technol. Lett. **15**, 882–884 (2003).

K. Zhang and D. Li, *Electromagnetic Theory for Microwaves and Optoelectronics 2nd Edition*, 2007 Springer, New York.

Z. Zhang, X. Bao, Q. Yu, L. Chen, "Fast state of polarization and PMD drift in submarine fibers," IEEE Photon. Technol. Lett. **18**, 1034–1036 (2006).

Z. Zhang and X. Bao, "Distributed optical fiber vibration sensor based on spectrum analysis of Polarization-OTDR system," Opt. Exp. **16**, 10240–10247 (2008).

Publications

J. Leeson, X. Bao, A. Coté, "Polarization dynamics in optical ground wire (OPGW) network," Appl. Opt. **48**, 2214-2219 (2009).

X. Bao, J. Leeson, J. Snoody, L. Chen, "Fiber Sensor Applications in Dynamic Monitoring of Structures", Boundary Intrusion, Submarine and Optical Ground Wire Fibers", *Optical Fibre, New Developments* (2009).